Cement and Concrete Composites 166 (2026) 106396

Contents lists available at ScienceDirect

Cement and Concrete Composites

journal homepage: www.elsevier.com/locate/cemconcomp

A novel framework for realistic modelling of 3D mesostructure and fracture behaviour of recycled aggregate concrete

Yi Ding [a], Sadjad Naderi [b], Gert van der Heijden [a], Mingzhong Zhang [a,*]

[a] Department of Civil, Environmental and Geomatic Engineering, University College London, London, WC1E 6BT, United Kingdom
[b] Department of Aeronautics, Imperial College London, London, SW7 2AZ, United Kingdom

ARTICLE INFO

Keywords:
Recycled aggregate concrete
Irregular aggregate
Mesostructure
3D Voronoi tessellation
Cohesive zone model

ABSTRACT

Recycled aggregate concrete (RAC) offers a sustainable alternative to natural aggregate concrete, while its meso-scale modelling is often limited by overly simplified geometries. This study presents a novel 3D computational framework using Voronoi tessellation and hierarchical clustering to realistically generate 3D mesostructure of RAC. The model equips six distinct phases including old aggregate, old mortar, new mortar, two interfacial transition zones (ITZs) and voids, and employs splining and scaling techniques to control morphology. It produces irregular recycled aggregates with realistic size distribution, volume fraction, old mortar content, and shape descriptors in terms of sphericity, roundness and convexity. Validation indicates consistence with experimental findings in terms of geometry and composition. 3D meso-scale modelling of fracture processes in RAC under uniaxial compression can accurately capture the crack initiation at old ITZs and shear-dominated failure. The proposed modelling framework offers a robust tool for understanding the mesostructure-mechanical property relationships in RAC and optimising material design of RAC.

1. Introduction

The global construction industry generates vast amounts of construction and demolition (C&D) waste each year, contributing significantly to environmental pressures. At the same time, the demand for concrete and its primary raw materials (i.e., aggregates) continues to rise, with global aggregate consumption estimated at over 40 billion tonnes annually [1]. Countries such as China, India, and Australia each produce more than 100 million tonnes of C&D waste annually [2]. Recycled aggregate concrete (RAC) offers a sustainable and cost-effective alternative to conventional concrete by remanufacturing C&D waste into recycled aggregates (RA), which are then used to produce new concrete [3,4]. This can not only reduce the reliance on natural aggregates but also help mitigate the environmental impact of C&D waste.

The mechanical properties of RAC have been extensively investigated. The experimental studies indicate a significant influence of the properties of old mortar content [5–7] and interfacial transition zone (ITZ) [8] on mechanical properties of RAC such as compressive strength [8], tensile strength [9], flexural strength [10,11], and modulus of elasticity [8]. However, laboratory work cannot provide a whole picture of the internal heterogeneity [12] and damage evolution [13], as well as the role of ITZs in RAC [14,15]. As a complement, meso-scale modelling has been considered as a promising approach to exploring the mechanical behaviour of RAC accounting for its mesostructural characteristics [16,17]. As illustrated in Fig. 1, unlike natural aggregate concrete (NAC) that contains uniformly shaped aggregates embedded in mortar, RAC has a more intricate mesostructure, composed of old aggregates attached with old mortar and embedded within new mortar, resulting in multiple ITZs with varying characteristics [18]. Although the eight-phase models with old aggregate, new aggregate, old mortar, new mortar, and four ITZs have been proposed to represent this complexity [17], most existing studies adopt the simplified five-phase models for computational efficiency, including old aggregate, old ITZ between old aggregate and old mortar, old mortar, new ITZ between old mortar and new mortar, and new mortar [3,19–21]. These models are typically constructed using parametric geometry generation and take-and-place algorithms [13,22]. However, such approaches are constrained by geometric simplification and high computational cost and they fail to accurately reproduce the irregular morphology and heterogeneity of real RA.

A computationally efficient 3D meso-scale modelling framework that

* Corresponding author.
E-mail address: mingzhong.zhang@ucl.ac.uk (M. Zhang).

https://doi.org/10.1016/j.cemconcomp.2025.106396
Received 7 August 2025; Received in revised form 5 November 2025; Accepted 11 November 2025
Available online 13 November 2025

can accurately capture the irregular shape, layered composition and spatial distribution of RA in RAC is still lacking. As displayed in Fig. 2, in most models, the aggregates were regarded as 2D circular [8,17,23], elliptical [24], or polygonal aggregates [25] and only a few studies adopted 3D mesostructural models for RAC with mostly idealised spherical [21,26] or ellipsoidal [27] RA to simplify geometry generation. The proposed RAC models significantly oversimplify the physical geometry of RA [17,21,23–25,27–33]. The shape of RA has a significant effect on the mechanical behaviour [34] and durability [35,36] of RAC. Therefore, a realistic 3D mesostructural model that can accurately capture RA shape and size is essential for reliable meso-scale analysis and performance prediction [37,38]. Besides, the take-and-place method was generally used to generate RA in 3D, which requires significant iterations and calculations, particularly when ensuring compliance with a specified particle size distribution, e.g., a Fuller curve [39]. Ren et al. [40] found that over 200 placement attempts are needed for a single particle to achieve the expected particle size distribution. Due to the random nature of this process and the large number of particles in concrete, the detection of overlapping particles becomes computationally expensive, significantly increasing the processing time.

To overcome these shortcomings, a novel 3D meso-scale modelling framework for RAC based on Voronoi tessellation and dual-level hierarchical clustering is proposed here. The algorithm can generate non-overlapping, irregular particles with customizable geometry and phase composition. It supports six-phase mesostructure (old aggregate, old mortar, new mortar, two ITZs, and void) and enables precise control over particle shape, size, volume fraction, and old mortar content. The existing five-phase RAC models consisting of old aggregate, old ITZ, old mortar, new ITZ, and new mortar established based on parametric or take-and-place algorithms has some shortcomings: (1) Some studies on mechanical behaviour of RAC still use 2D plane that cannot fully capture the true spatial distribution, interlocking and orientation of irregular aggregates, as well as the complex 3D connectivity of cracks. 3D numerical modelling is undoubtedly a better choice, which enables the investigation of stress transfer, crack propagation, and failure mechanisms in all spatial directions. (2) Current 3D RAC models adopt idealised aggregate shapes such as spheres, ellipsoids and polygons, leading to limited geometric fidelity. (3) Universal old mortar morphology is added to evenly cover the old aggregates, as a result of which it is difficult to obtain a more accurate simulation of mechanical behaviour. (4) The overlap-detection and iterative placement processes required to achieve a target particle size distribution substantially increase the computational cost, particularly when high aggregate volume fractions are involved. The proposed six-phase model that introduces an additional void phase increases the physical realism and adopts a Voronoi-based hierarchical clustering strategy. This approach directly generates non-overlapping, irregular aggregates with controlled morphology, old-mortar content, and void distribution, thereby enhancing geometric realism and computational efficiency while removing the need for iterative placement loops. The proposed framework can therefore achieve: (1) realistic particle representation that accurately captures the irregular morphology of RA; (2) efficient handling of multi-phase materials, including two distinct ITZs and voids; (3) robust control of particle size distribution consistent with sieve analysis data; (4) strong alignment with experimental observations in terms of shape descriptors and old-mortar content; (5) high configurational flexibility that allows independent tuning of aggregate shape, size and volume fractions; and (6) realistic and accurate simulations of fracture behaviour in terms of internal crack initiation and propagation.

The novelty of this research lies in the development of a novel 3D meso-scale modelling framework for RAC, which integrates the realistic irregular particle morphology, variable old mortar layering, and highly flexible geometric parameters that has not been proposed in existing studies. The newly added old mortar layer provides flexibility in controlling the old mortar content, thereby allowing adjustments to the size and shape of RA. Additionally, voids are incorporated to make the model more realistic. The resulting RAC model aligns well with experimental results in the literature, particularly in terms of shape, size, and old mortar content. The shape and size of each individual old aggregate and RA as well as old mortar content can be fully customized, facilitating

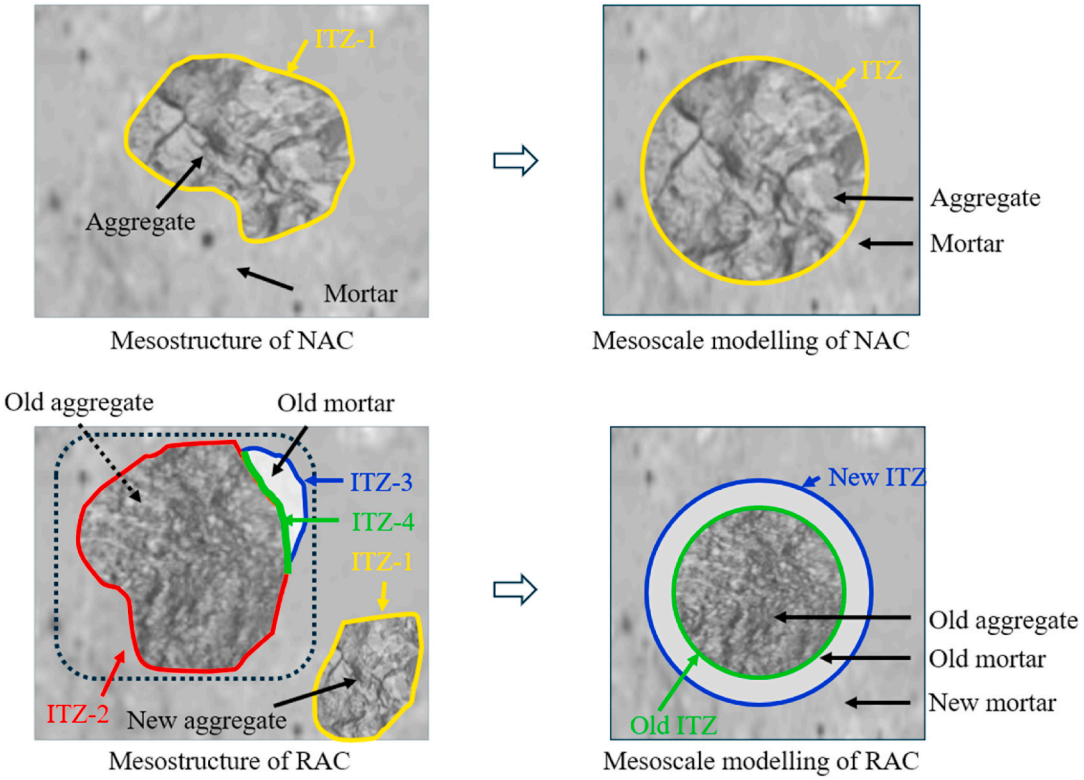

Fig. 1. A comparison of mesostructure and meso-scale models between NAC and RAC.

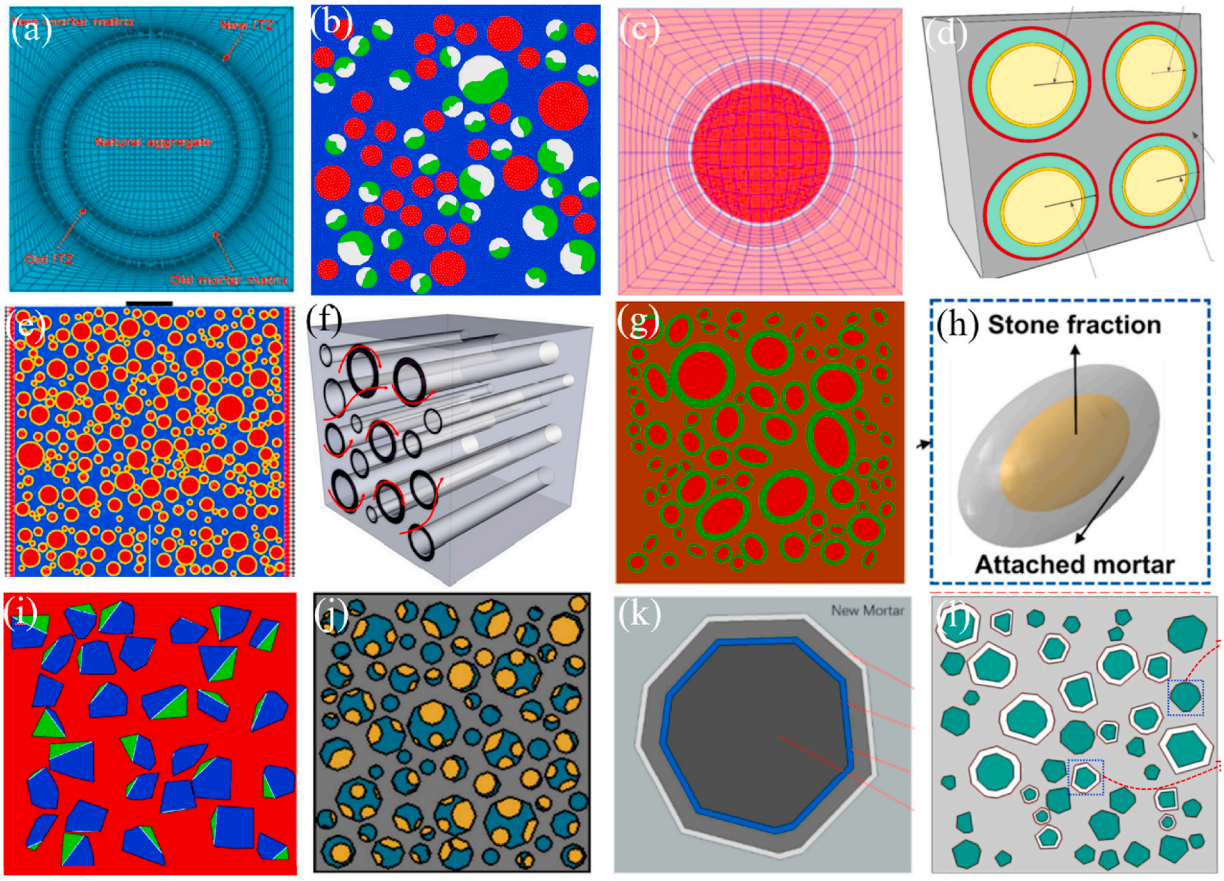

Fig. 2. A summary of the existing mesostructural models of RAC considering the recycled aggregates as: (a)–(f) circle [8,17,21,23,26,32], (g)–(h) ellipse [24,27], and (i)–(l) polygon [25,28,30,42].

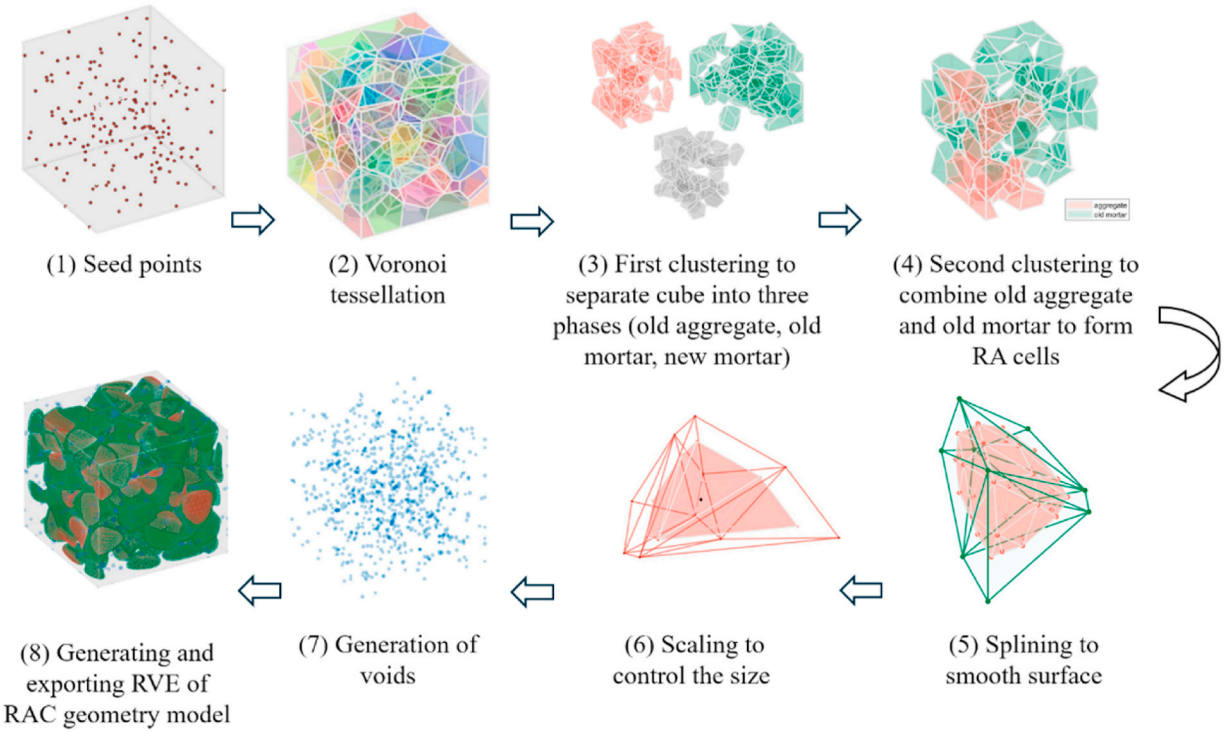

Fig. 3. Schematic illustration of the procedure for generating 3D geometry of RAC.

future sensitivity analyses. To date, no research has adopted a 3D irregular RA model with an uneven old mortar layer for meso-scale studies of physical and mechanical behaviour of RAC. By providing a systematic methodology for constructing detailed and flexible geometric models, this approach supports the development of highly realistic 3D mesostructure models of RAC. As part of a larger research project, the models developed in this study can subsequently be used for finite element analysis (FEA) of RAC performance under various loading and environmental conditions considering its mesostructural characteristics.

2. 3D geometry model of recycled aggregate concrete (RAC)

Fig. 3 illustrates the procedure for modelling RAC geometry using the proposed 3D Voronoi tessellation-based framework, which mainly includes eight steps: (1) Generation of seeding points within a predefined cuboidal domain; (2) Formation of Voronoi cells by the seeds; (3) First clustering of Voronoi cells to separate the three phases within RAC, i.e., old aggregate, old mortar, and new mortar; (4) Second clustering to form recycled aggregate cells; (5) Application of splining techniques to smooth the geometry of aggregates; (6) Adjusting the single particle size by scaling and controlling the global size distribution by iterations; (7) Generation of voids in RAC; (8) Generating and exporting representative volume element (RVE) model of RAC. More details about each step are given below.

2.1. Systematic design of seed points and Voronoi cells

Voronoi tessellation was adopted as a discretisation technique to segment the cube into distinct regions for subsequent operations. The process of generating Voronoi cells has been described in detail in a previous study [43]. This approach partitions space based on seed points, resulting in non-overlapping polyhedral cells that collectively fill the domain. Each Voronoi cell is defined by proximity to a specific seed point. This method effectively represents irregular particle geometry and distribution, making it particularly valuable for modelling the 3D mesostructure of heterogeneous materials like concrete [43–46].

The following outlines the approach for systematically generating and manipulating 3D points within a defined cuboidal space. To approximate the number of seed points, the distance between the seeds is initially designed to be evenly distributed, and then random is used to control the distance between the seeds to achieve the randomness of the distribution. By controlling the level of irregularity, the shape and size are also locally governed by the relative distances between seed points and their positions are in relation to one another. The more irregular and random the Voronoi cell, the higher the randomness of the particles' size, shape and position that will be generated later. Fig. 4 gives an example of going from highly randomized seed points to generating a Voronoi cell. More detailed steps of seed distribution adjustment and various generation results can be found in a previous study [43].

2.2. First-level clustering of Voronoi cells

The tessellated cubic domain is then discretised into three distinct phases: aggregates, old mortar, and new mortar. The key is to systematically cluster the Voronoi cells so that the total volume fraction of each cluster closely approximates the corresponding phases. The first clustering focuses on the three main phases (i.e., old aggregate, old mortar, and new mortar) to predefined volume fractions, as shown in Fig. 5. The generation of the other phases will be discussed later.

Fig. 6 presents a flowchart of first clustering, indicating the process of clustering Voronoi cells into three distinct phases, guided by predefined volume fractions. The process begins with the identification of neighbouring Voronoi cells by iterating through all cells and comparing them pairwise to determine shared vertices. Two cells are considered neighbours if they share three or more vertices. Once the neighbouring cells are identified, they are recorded and used for subsequent clustering. The clustering starts by selecting a random Voronoi cell for the first phase and adding neighbouring cells iteratively until the total volume of the selected cells reaches or exceeds the required volume for that phase. After achieving the required volume, the algorithm moves to the second phase. Again, neighbouring cells from the first phase are selected, and cells are added until the second phase volume meets the target requirement. The process continues until the third phase, where any remaining cells that have not been assigned to the first or second phases are automatically allocated. This method ensures that each phase occupies its intended volume fraction within the overall structure.

2.3. Second-level clustering of Voronoi cells

The second clustering aims to generate the RA particles in RAC by merging the aggregate and old mortar phases. The key step is to find the old aggregate neighbouring cells from the old mortar cells and delete the adjacent faces to form the new particle that is the RA cell including old aggregate and old mortar. A flowchart of second clustering for RA is given in Fig. 7.

Fig. 8 demonstrates an example of the second clustering steps for an individual RA in RAC. The process begins by systematically organising the cells within each phase according to their volumes. Specifically, after the initial separation of cells into different phases (e.g., aggregate and mortar), each set of cells is sorted by volume. This step is essential because it allows for a more controlled and orderly approach to subsequent clustering. By addressing the smaller cells first, the process

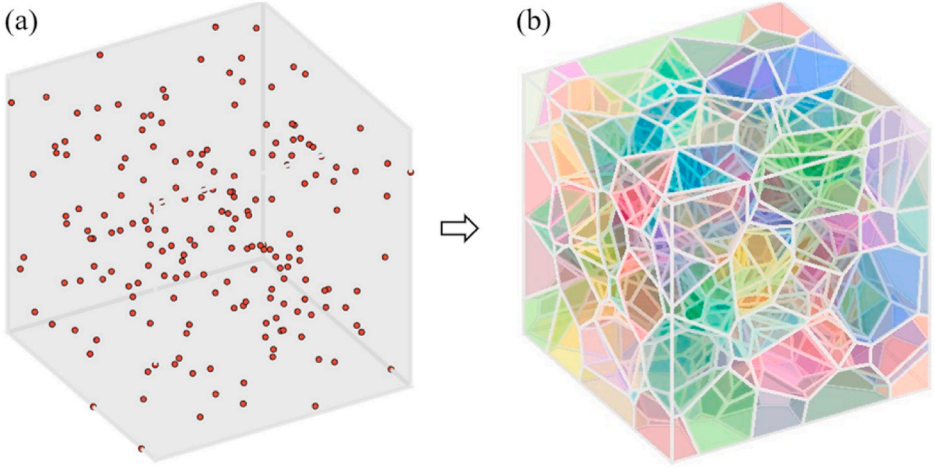

Fig. 4. (a) Seeding points and (b) generating Voronoi cells from the seeds.

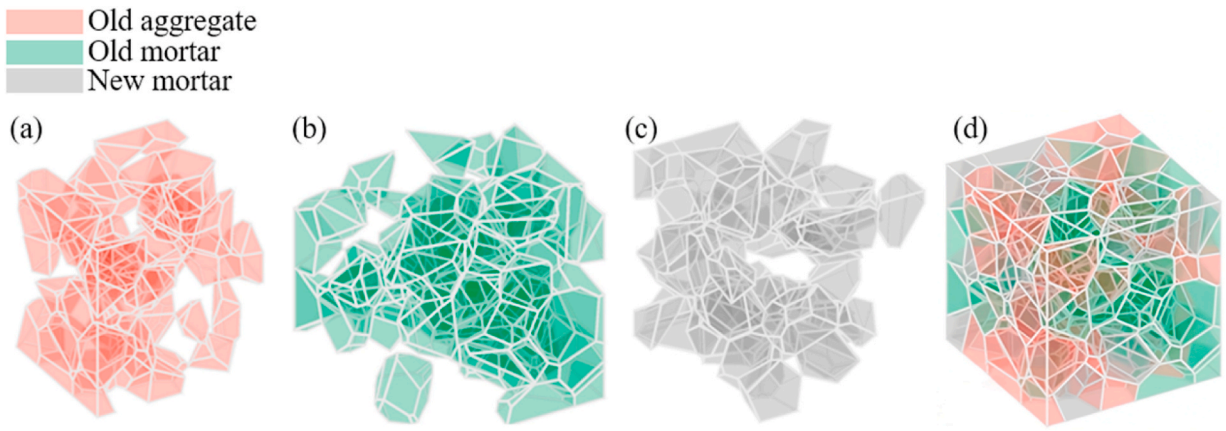

Fig. 5. Clustering Voronoi cells for proportion of three phases (aggregate, old mortar, new mortar): (a) 10 % old aggregate, (b) 20 % old mortar, (c) 70 % new mortar, and (d) the three phases in the domain of concrete.

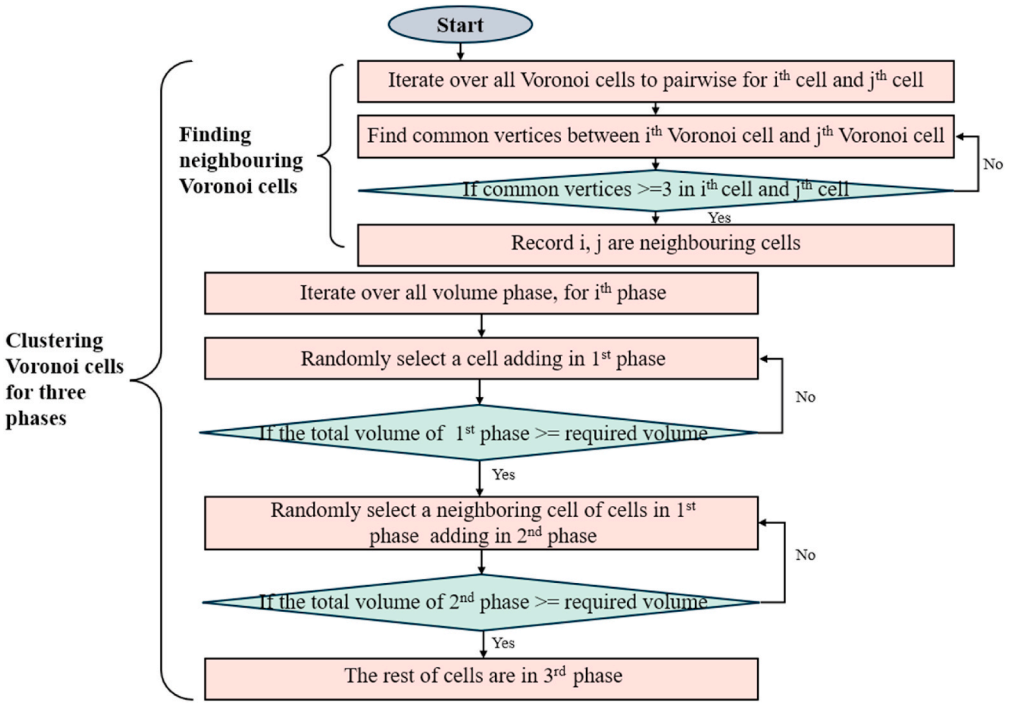

Fig. 6. A flowchart for the first-level clustering of three phases in RAC.

minimises the risk of leaving larger ungrouped spaces and ensures a more efficient allocation of cells. Once the cells are sorted by volume, the next step is to cluster them into groups. Clustering is based on the spatial proximity of the cells to meet the volume criterion: (1) The clustering starts by attempting to pair cells from different phases that are spatially adjacent to one another. That is, an aggregate cell is paired with a neighbouring mortar cell. The pairing process is conducted methodically, starting from the smallest aggregate cells and checking which of their neighbouring cells belong to the mortar phase. If a suitable neighbouring cell is found, and it has not already been assigned, then it is grouped with the aggregate cell. This ensures that the clustering process is organised and avoids repeated placing the cells. (2) After the primary clustering, some old mortar cells may remain unpaired. Any old mortar cells that were not included in the initial clusters are randomly assigned to the existing clusters. It is important to note that the allocation of these unused old mortar units to the formed RA clusters is employed according to its neighbouring relationship. That is, the unused old mortar units are added to the neighbouring formed RA clusters to get new RA clusters.

The interfaces between the old aggregate cell and the mortar cell need to be identified and removed to form a unified RA cell. Later, this allows these faces to be excluded from the splining process, making it easier to generate a continuous mesh across cells within a cluster. To identify and remove interfaces between adjacent Voronoi cells, the following systematic workflow was applied: (1) Firstly, identifying adjacent cells by examining neighbouring relationships among seed points and creating a list of cells that share boundaries with each Voronoi cell. (2) For each pair of adjacent cells, shared faces are detected by identifying common vertices and edges that define the interface. These shared faces are validated to ensure that they accurately represent boundaries between the two cells. (3) Once identified, shared faces are deleted directly without altering the shape of the remaining geometry, ensuring that only the interface is removed while preserving the distinct structure of each cell. (4) After deleting these shared faces, the geometric data structure is updated. (5) Finally, a new diagram is generated for confirmation after merging interfaces, ensuring the interface is removed

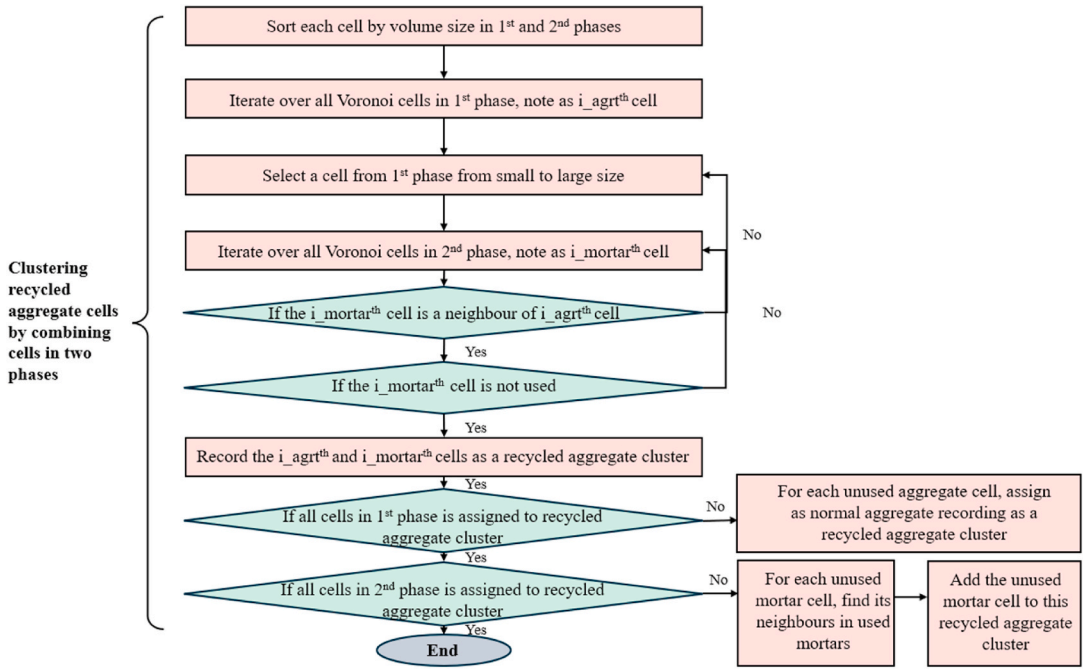

Fig. 7. A flowchart for the second-level clustering of recycled aggregates in RAC.

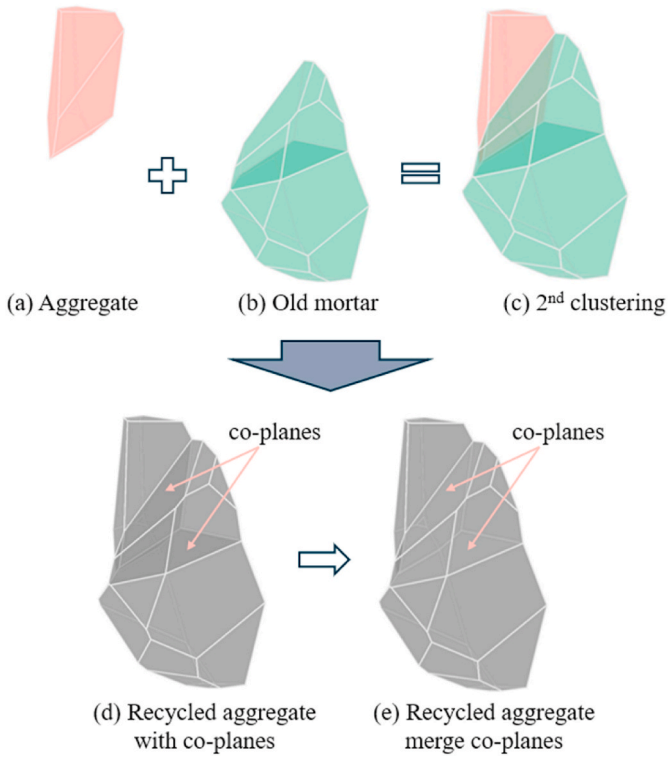

Fig. 8. Second clustering steps for an individual recycled aggregate.

from each merged cell and no gaps are introduced during the deletion process.

2.4. Scaling process

A computational method was proposed to simulate the shrinkage of particles within a material. The method begins by defining different shrinkage ratios for particle aggregates and ITZ, representing varying degrees of dimensional reduction. The scale factor must be in the range of 0–1, aiming to shrink particles to prevent overlapping with the neighbouring cells. The core strategy involves setting the shrinkage ratio for old aggregates to be smaller than that for the old ITZ, and similarly, the ratio for RA is set smaller than that for the new ITZ. This approach ensures that the old ITZ encapsulates the old aggregate, while the new ITZ envelops RA. The centroid of each polygon is then calculated by averaging the 3D coordinates of the vertices. Using the predefined shrinkage ratios, each vertex is scaled inward toward the centroid, effectively reducing the particle's size by adjusting the vector from the centroid to each vertex (Fig. 9). The scaled cell volume and shape characteristics are saved for global size distribution adjustment.

2.5. Splining process

The proposed splining technique builds on the Loop subdivision surface method that is a technique developed by Charles Loop [51] for refining triangular meshes. Its core purpose is to enhance mesh smoothness and detail by subdividing each triangular face into smaller triangles. Key steps for the splining process can be found in a previous study [43]. Fig. 10 illustrates the process, by which a single particle

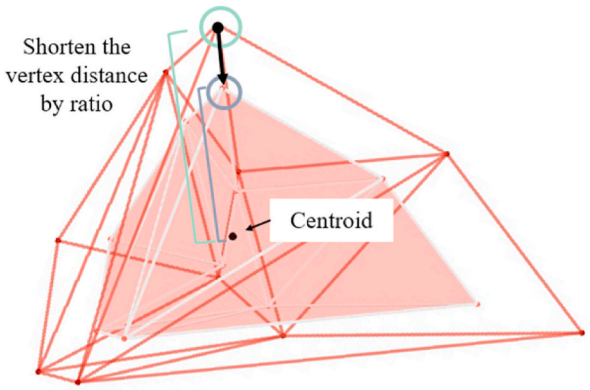

Fig. 9. A scaling particle with centroid.

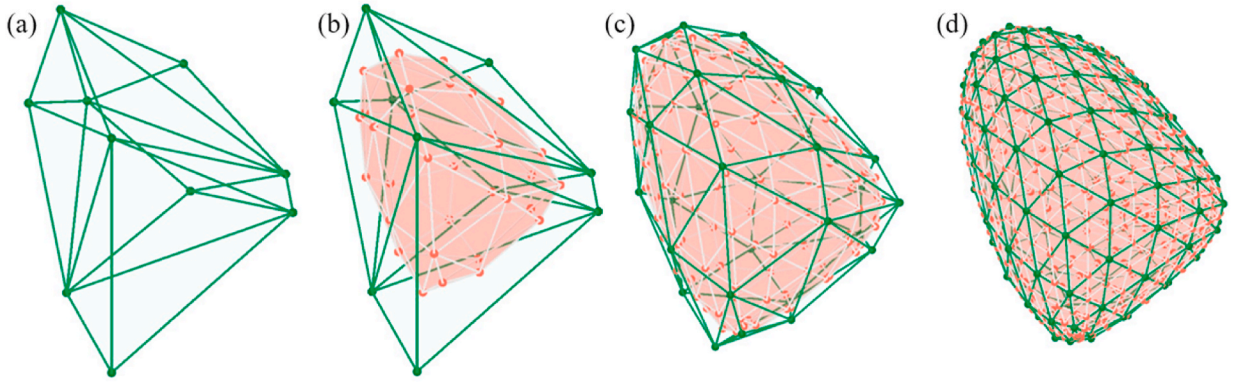

Fig. 10. Loop subdivision process: (a) Voronoi cell, (b) first iteration, (c) second iteration, and (d) third iteration.

achieves a smoother surface with each iteration. By increasing the number of subdivision iterations, a highly smooth surface can be obtained. However, it should be noted that this method significantly increases triangle counts, and thus would lead to more solid elements and a rise in computational cost of FEA.

2.6. Generation of voids

The voids are generated based on the vertices in second clustering cells. The procedure of generation of voids is illustrated in Fig. 11, which are based on the results of RA Voronoi cells obtained after the second clustering (Fig. 11(a)). The vertices of the combined Voronoi cell serve as seed points for the generation of spheres of varying sizes (Fig. 11(b)). Based on these seed points, a predetermined number of spheres are randomly selected and generated at the vertex coordinates. The spheres will overlap with the cells if their radii exceed a certain value, meaning sphere size adjustment is only possible within a limited range. The maximum limit of radius of inserting sphere needs to be determined by calculating the distance between the Voronoi cell vertices and the generated surfaces after splining process (Fig. 12).

The vertices of the original Voronoi cell and the vertices of the triangle mesh generated after the splining process are already in the database, so they only need to be called for computation. To calculate the shortest distance between a point and a set of triangular surfaces, the following steps are employed:

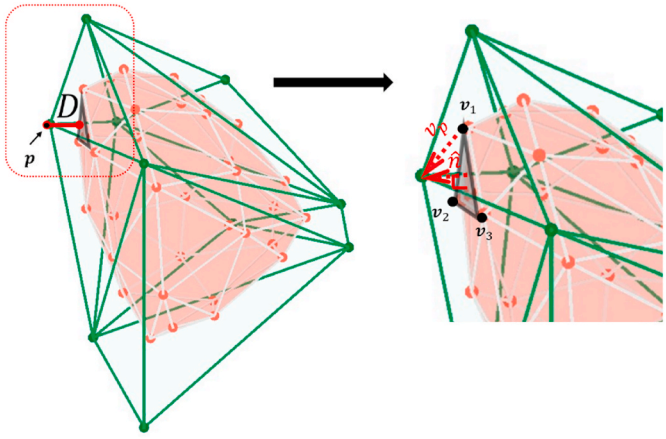

Fig. 12. A schematic diagram of parameters used for calculating the range of inserting sphere.

(1) Extracting the three points coordinates of each triangle face and calculating the normal vector of each face. The normal vector n is the cross product of two edge vectors of the triangle:

$$n = (v_2 - v_1) \times (v_3 - v_1) \tag{1}$$

The normal vector is normalized to get a unit normal vector $\hat{n}$:

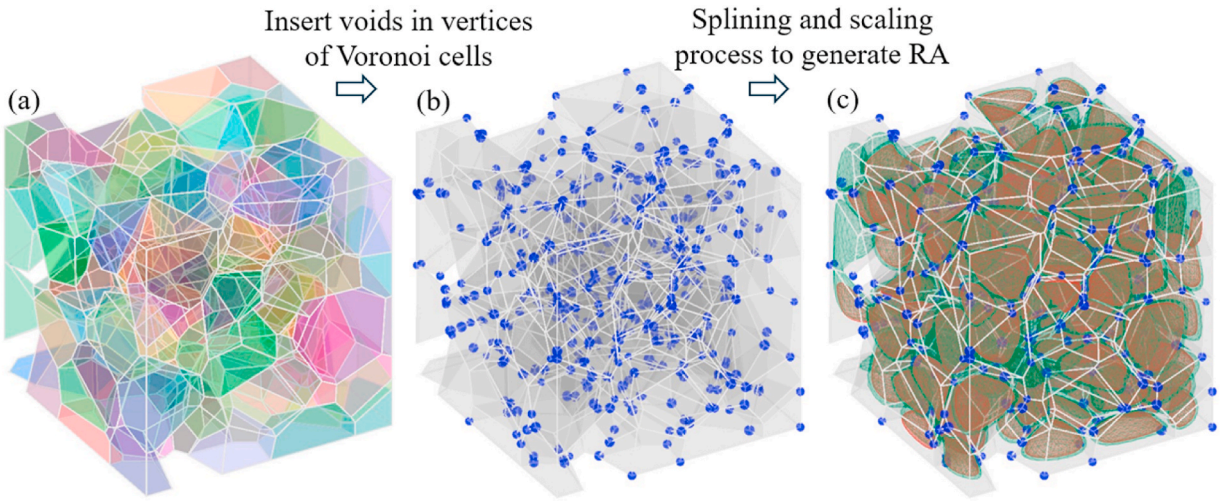

Fig. 11. A schematic illustration of the procedure for generating voids: (a) RA Voronoi cells; (b) Inserting random voids at vertices of Voronoi cells; (c) Splining and scaling to generate RA particles within the boundary of Voronoi cells.

$$\hat{n} = \frac{n}{|n|} \tag{2}$$

(2) Calculating the vector from the one vertex in triangle to the query point in the Voronoi cell. Choose one vertex of the triangle (for example, v_1) and compute the vector from this vertex to the point p:

$$v_p = p - v_1 \tag{3}$$

(3) Computing the distance to the plane of the surface. The dot product of vector (obtained in step 2) and the normal vector of the face gives the signed distance from the point to the plane defined by each face. The perpendicular distance D from the point p to the plane of the triangle is the dot product of v_p and the unit normal vector $\hat{n}$:

$$D = |v_p \cdot \hat{n}| \tag{4}$$

where v_1, v_2, v_3 are the vertices of the triangle, p is the point, $\hat{n}$ is the normalized normal vector of the plane, and D is the perpendicular distance from the point to the plane containing the triangle.

(4) For each vertex of the Voronoi cell, by traversing the triangle mesh, the face with the smallest absolute distance to the point is selected. As a result, the minimum distance is recorded as the maximum of the resulting sphere radius for each vertex.

As the aggregate size is smoothed and reduced in size based on the cell structure, the generated spheres do not overlap with the aggregates (Fig. 11(c)). The average volume of the spheres can be calculated as:

$$V_{avg} = \frac{V_{total} \times \text{Porosity}}{N_{spheres}} \tag{5}$$

where V_{avg} is the average volume of the spheres, V_{total} is the total volume of the material, and $N_{spheres}$ is the number of spheres.

The radius of each sphere can then be determined using the sphere volume formula. Random variations in the radius of the sphere can be introduced to simulate the random distribution of void sizes and to ensure that the maximum diameter of the sphere needs to be within the range of the above distance calculations to avoid overlap.

In this study, 1124 vertices were randomly chosen for generating voids from Voronoi diagram. The spheres with diameters of 1–5 mm were inserted to simulate a 2 % volume fraction of voids, as per the X-ray CT experimental data [47]. The most commonly used hierarchical adjustment method was employed to contribute the void size distribution, which requires defining the target volume fraction for different size ranges and then adjusting them through an iterative algorithm [43,48]. A detailed description of the void size control algorithm was provided in Section 3.1.1. Table 1 gives the size distribution of voids with three size ranges adopted in this study. A comparison of the size distribution of voids between simulations and experimental data is displayed Fig. 13.

Using the vertices of Voronoi cells as centres of voids is a method to improve efficiency in determining positions, which can be achieved by calling upon previously collected data with no need to select positions and conduct geometric overlap detection. This method can generate voids with random distribution and avoid geometrically overlapping between voids and aggregates. However, more complex void distribution needs further investigations for the scenarios that voids also exist within the OM phase and tend to concentrate near the boundaries of old mortar where compaction efficiency is reduced.

Table 1
Size distribution of voids in RAC.

Void size range (mm)	Expected frequency (%) [47]	Modelling frequency (%)
0–1	0.8	0.793
1–2	0.15	0.145
2–5	0.05	0.062

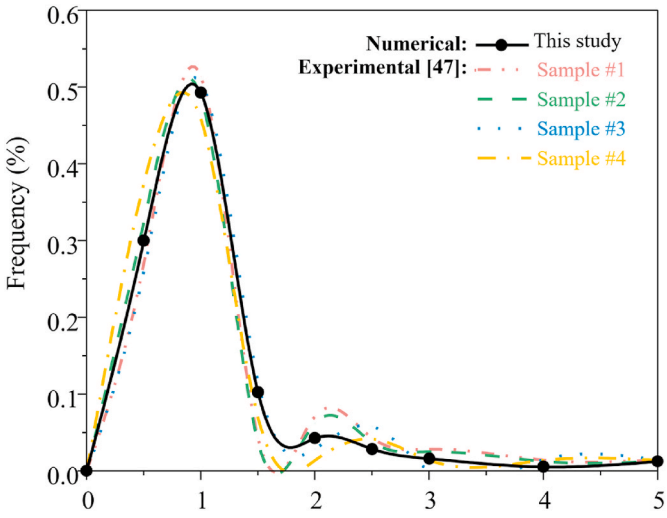

Fig. 13. A comparison of simulated and experimental size distribution of voids in RAC.

2.7. 3D mesostructure

Fig. 14 demonstrates the generated 3D mesostructure model of RAC, which was represented by a triangulated surface mesh. The coordinates of all nodes, along with face connectivity data, are stored for potential modifications and refinements in later stages. This data structure is compatible with common FEA workflows. To facilitate integration with various FEA platforms, the model can be exported in STL format, which provides a standard triangulated surface representation of the 3D geometry. The STL file format is widely supported by FEA software such as COMSOL and ABAQUS. Within these platforms, the imported triangulated surfaces can be used to construct solid elements through appropriate meshing techniques, enabling further mechanical or structural simulations based on the generated 3D mesostructure.

3. Size and shape configurations

3.1. Recycled aggregate

3.1.1. Particle size distribution

The particle size distribution (PSD) of RA was taken as input to design both the seeding point systems and configuration of particle sizes effectively. The potential number of particles serves as an estimate for the total number of seeding points. The particle count for each size can be calculated by dividing the representative volume of a particle by the total volume for that size category. For irregularly shaped RA particles, the representative volume is equivalent to the volume of a sphere with the same size, where the radius of the sphere is used as the size descriptor. If the volume of the irregular particle is denoted as V, the equivalent radius R_{eq} can be determined as:

$$R_{eq} = \sqrt[3]{\frac{3V}{4\pi}} \tag{6}$$

PSD is commonly determined through sieve analysis, particularly for materials like concrete containing randomly shaped aggregates. This method quantifies the mass fraction of particles within defined size

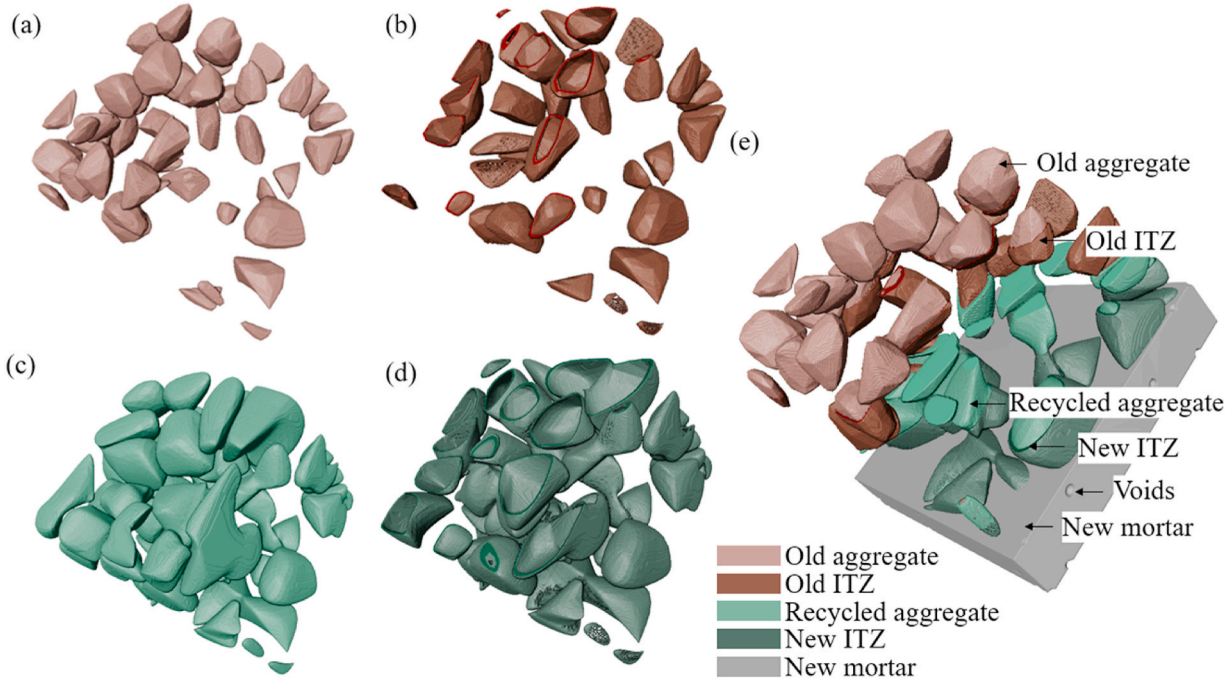

Fig. 14. 3D mesostructure of RAC including individual and cross-section view of multiple phases: (a) old aggregate; (b) old ITZ; (c) recycled aggregate; (d) new ITZ; (e) RAC with voids.

intervals and enables the development of a cumulative distribution curve. Aggregate gradation design is based on the Fuller curve to obtain the optimal concrete mix design, as expressed by Ref. [41]:

$$\mathscr{P}(d) = 100\left(\frac{d}{d_{max}}\right)^{a} \tag{7}$$

where $\mathscr{P}(d)$ denotes the cumulative percentage of particles passing through a sieve with an aperture diameter d, $d_{\max}$ is the maximum size of the aggregates, and a is a constant (typically ranging from 0.45 to 0.70).

To facilitate the numerical implementation, the gradation curve described by Eq. (7) is segmented. The volume of aggregate V_{agg} within the grading segment $[d_i, d_{i+1}]$ can be calculated as [39]:

$$V_{\text{agg}}[d_i, d_{i+1}] = \frac{\mathscr{P}(d_{i+1}) - \mathscr{P}(d_i)}{\mathscr{P}(d_{\max}) - \mathscr{P}(d_{\min})} \times \mathscr{P}_{agg} \times V_{tot} \tag{8}$$

where $d_{\min}$ denotes the minimum size of the aggregates, $\mathscr{P}_{agg}$ stands for the volume fraction of the aggregate, and V_{tot} is the total volume of the specimen.

Based on experimental data, the calibration is conducted to ensure the acceptable minimum and maximum particle volumes for each size range within the target PSD, following the detailed configuration procedure given in the literature [43]. For particle generation using the Voronoi tessellation method, oversized particles can be easily adjusted by applying a uniform scaling process to reduce their dimensions while maintaining their shape characteristics. However, if the generated particles are smaller than the required size range, the initial seeding points must be redefined, and the entire mesostructure generation process must be repeated. This ensures that the final particle size distribution closely matches the target specification. Instead of controlling a single particle, in the 3D mesostructure model of RAC, we need to control the size of RA that are cells from two phases (old aggregate and old mortar), suggesting more flexibility to adjust the size. If the generated RA particles are too large, the scaling process can be used to reduce the size of a single RA more easily. If the generated RA particles are too small, the old aggregate and old mortar can be recombined to produce new RA particles. As mentioned earlier, old aggregates are usually accompanied by multiple adjacent old mortar cells. If a certain RA is smaller than the required RA, the old mortar cell of this RA can be adjusted separately, and a larger old mortar cell is selected to combine with the old aggregate to form a new RA to achieve the required size. If the size is still too small after adjusting the old mortar, the seed points are redistributed for calculation. As the single RA size can be adjusted through the second clustering process, the single RA size can be controlled more precisely and the number of iterative operations required to reconstruct the model can be reduced. Changing old mortar cells usually solves most particle size problems. For the generation of 80 RA particles, the PSD consistent with the experimental data can be basically obtained within two iterations.

Fig. 15 presents a flowchart with key steps of controlling the PSD of RA. Compared to the conventional take-and-place approaches, the Voronoi-tessellation based approach offers several advantages, including increased volume fraction and reduced computational cost. Using take-and-place method is difficult to achieve high volume fractions for polyhedral aggregate particles [22]. It is worth noting that the model generated based on Voronoi's method avoids overlapping problems in the PSD calibration process. Therefore, there is no process of repeated placement of aggregates to achieve high volume fractions, and there is no overlap detection and iterative placement after overlap. The RA size can be controlled by scaling to shrink, or clustering to enlarge. This method is theoretically more efficient and convergent. It is worth noting that the method was specifically designed for calibration using sieve analysis data, although it can be employed for other types of particle size interpretations. Probability density functions were adopted as measurement data to refine the size of Voronoi cells.

Using experimental data in the literature [49] as an example, the proposed model can generate a consistent PSD curve with the experiment. The Voronoi cells were generated by seeding points inside a square with a side length of 100 mm. The randomness of the points was set to 0.1 to ensure that the seeds have enough randomness to meet the grading requirements of the aggregates, and the results are controllable. The initial shrinking factor was set to 0.8, and two splining process treatments were used to smooth the surface of the particles. Then, the particles were graded in 10 size ranges of diameter from 22.5 mm for coarse aggregates to 0.2 mm for fine aggregates. Then, based on the

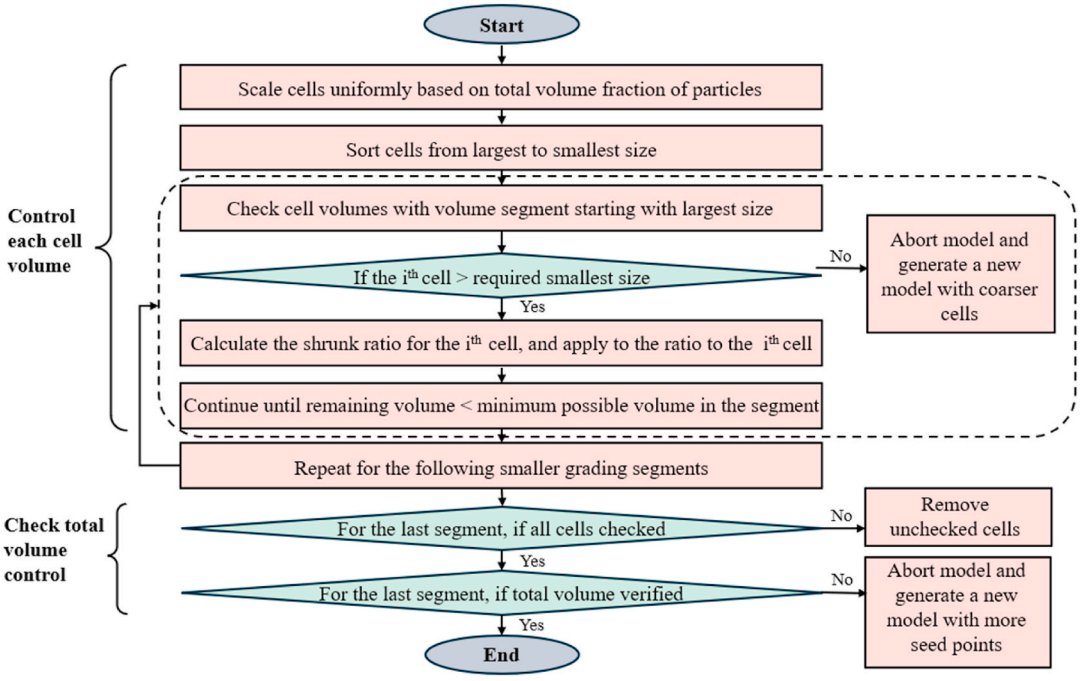

Fig. 15. A flowchart of controlling the particle size of RA.

above-mentioned flowchart, the size of a single particle was further controlled and refined. Separating the more size segments contributed to a more accurate size control, and the simulated PSD can be closer to the desired curve. 8 size segments were used to achieve this purpose.

The convergence of the iterative PSD calibration was evaluated by comparing the simulated cumulative passing volume with the target experimental data. When the cumulative percentage within the specified particle size range deviated by no more than ±5 % from the experimental data, convergence was considered to be acceptable. Three examples with various seeding points (54, 128 and 250 seeds) were taken for PSD fitting to validate the robustness and universality of such size control algorithm. All these cases reached the expected PSD within 5 % tolerance in two iterations. For mixtures with larger gradation ranges, convergence may require more iterations to achieve. The simulation

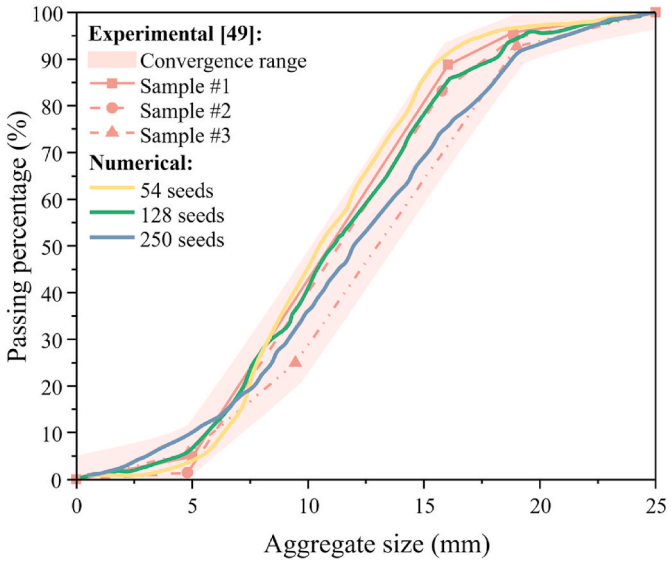

Fig. 16. A comparison of simulated and experimental particle size distribution of RA.

results of PSD were in good agreement with experimental data, where all the volume fractions of aggregates were over 35 % (i.e., 36.5 % for 54 seeds, 41.8 % for 128 seeds, and 43.2 % for 250 seeds), within the reasonable value for RAC. Figs. 16 and 17 display a comparison of the simulated and experimental PSD of RA and the generated RA particles after PSD fitting, respectively. The coefficient of determination (R^2) and the root mean square error (RMSE) were adopted to evaluate the scatter between simulations and experimental data in terms of passing percentages which were calculated based on the average value of three experimental samples for the passing percentages in different sieving sizes, as presented in Table 2 for the three cases with 54, 128 and 250 seeds. The size ranges followed the sieve data given in BS EN 933–1 [50]. The simulations achieved $R^2 > 0.95$ and RMSE <5 %, indicating a good agreement with experimental data and confirming the feasibility of using the proposed iterative PSD calibration method to accurately reproduce experimental grading distribution within acceptable tolerance. As seen in Fig. 16, although the PSD curves for all three cases fit the experimental data within a 5 % error margin, models with fewer seed points tended to produce larger particles, whereas those with more seed points yielded smaller particles. The model with 128 seeds provided the best agreement with experimental data and thus was selected for the subsequent numerical analyses.

3.1.2. *Particle shape adjustment*

Fig. 18 shows the comparisons between the simulated RA particles and the measured realistic RA particles from experiments [33], indicating that the simulated particles are very close to the real aggregate in terms of shape. The shape of Voronoi cells is influenced by both the seeding points and the splining process. These shape variations can be quantitatively assessed using parameters such as sphericity (S_p), roundness (R_n), and convexity index (κ). S_p is primarily used to evaluate the overall shape of the cell, measuring how much a particle deviates from an ideal sphere. It can be calculated based on the particle's volume (V) and surface area (S). V is determined using MATLAB's built-in volume function, which requires the cell to be meshed with artificial solid elements solely for volume computation, without incorporating them into the final model. S is the sum of the area of each patched face. Thus, S_p can be calculated as:

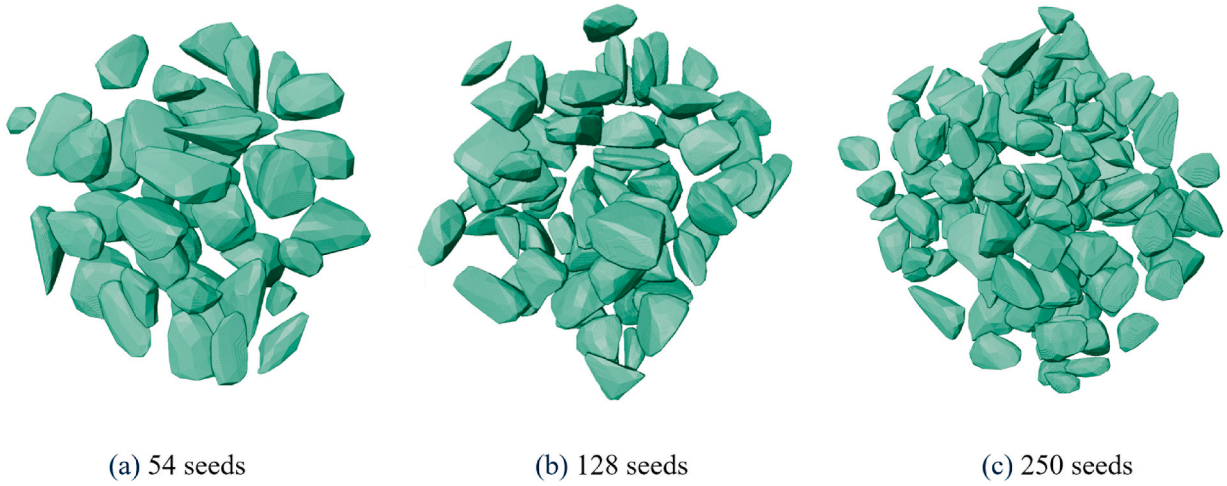

Fig. 17. Visualisation of simulated RA particles with PSD consistent with experimental data: (a) 54 seeds; (b) 128 seeds; (c) 250 seeds.

Table 2
Quantitative comparison between simulated and experimental passing percentages of RA particles with various seed numbers.

Sieve size (mm)	Passing percentage (%) for 54 seeds	Passing percentage (%) for 128 seeds	Passing percentage (%) for 250 seeds	Experimental passing percentage (%) [49]
4.0	2.213	4.267	7.467	2.503
5.6	5.763	9.761	12.501	10.757
8.0	27.231	27.876	23.669	31.927
11.2	55.245	50.478	44.186	55.134
16.0	91.546	85.376	75.037	88.106
22.4	98.245	97.654	97.436	97.986
25.0	100.000	100.000	100.000	100.000
R^2	0.9866	0.9984	0.9887	1
RMSE (%)	4.4432	1.5399	4.08	0

$$S_p = \frac{\text{Surface Area of Equivalent Sphere}}{\text{Surface Area of Particle}} = \frac{4\pi\left(\frac{3V}{4\pi}\right)^{2/3}}{S} \tag{9}$$

The local shape of aggregates is examined using R_n and κ. There are various methods for assessing R_n, which can be determined by calculating the angle between the surface position vector r and the unit normal vector $\hat{u}$ [51]. In a triangulated mesh, r represents the vector from the cell centre to the centroid of a triangular surface element, while $\hat{u}$ is the corresponding normal vector. The angle between r and $\hat{u}$ is calculated using $\hat{r}\cdot\hat{u}$, where $\hat{r} = \frac{r}{|r|}$. R_n is then defined as a weighted average, considering the surface area of each triangular element, as follows:

$$R_n = \frac{\int_S |\hat{r}\cdot\hat{u}|dS}{\int_S dS} \approx \frac{\sum_{i=1}^{m} |\hat{r}_i\cdot\hat{u}_i|\Delta S_i}{S} \tag{10}$$

After the splining process, the potential creation of concave surfaces is evaluated by the convexity index (κ), which is typically calculated as the ratio of the particle's volume (V) to the volume of its convex hull (V_{conv}) with the latter computed using MATLAB's convhull function, as follows [52]:

$$\kappa = \frac{V}{V_{conv}} \tag{11}$$

All indicators are in the range of 0–1. R_n and S_p of 1 represent a perfectly spherical shape. When κ is 1, it indicates that the particle remains unchanged from the original Voronoi cell, so that the convexity is kept the same. The aggregates in Fig. 18 are sorted by irregularity. The three shape parameters, i.e., sphericity (S_p), roundness (R_n) and convexity (κ), drop with increasing irregularity. The smoother and closer to the ideal sphere, the higher sphericity, roundness and convexity of the particle. The three parameters equal to 1 indicates that the shape is a smooth sphere.

Fig. 19 presents an example of the parametric analysis with 450 generated RA particles. More particles are generated to avoid accidental outliers affecting the accuracy of the statistical results. R_n and S_p exhibit an approximately normal distribution, with lower and higher values being relatively sparse and most data clustering near the median. Most particles' sphericity parameters centre around 0.8, ranging from 0.6 to 1. Similarity, most particle roundness values concentrate around 0.5, within the range of 0–0.9. This suggests that aggregate irregularity follows a nearly normal pattern, with few particles exhibiting extreme angularity or near-spherical shapes, while the majority lie between spherical and highly irregular shapes. Regarding κ, most data points fall between 0.9 and 1, indicating minimal deformation from the original Voronoi cell to the generated particle, with only a small number exhibiting significant changes in κ. Excluding the last convexity column, i.e., excluding the particles with less shape change, the remaining data of particles with altered κ also show the characteristics of normal distribution. The simulated particle shapes in terms of sphericity, roundness and convexity are consistent with the real shapes of coarse aggregates in concrete [51].

3.2. Mortar

As seen in Fig. 20, a single cell can combine with various neighbouring cells to form the four different RAs, and the old mortar content is calculated for each RA. Experimental studies have reported that the old mortar content in RAC typically varies from 14.3 % to 63.8 %, depending on factors such as the quality of the parent concrete, the crushing method, and the recycling processes employed [6,53,54]. It is essential to accurately replicate this variability for meso-scale modelling considering the heterogeneity and mechanical response of RAC.

In this study, a Voronoi tessellation-based modelling framework was employed, wherein 189 seed points were randomly distributed to generate the initial aggregate geometry. The target old mortar content was controlled through three key modelling strategies: (1) By adjusting the initial clustering volume ratios for old aggregate (OA), old mortar (OM), and new mortar (NM) phases (Fig. 21), the volume fraction and spatial distribution of old mortar could be significantly altered. (2) Modifying the secondary clustering schemes (Fig. 22) allowed further

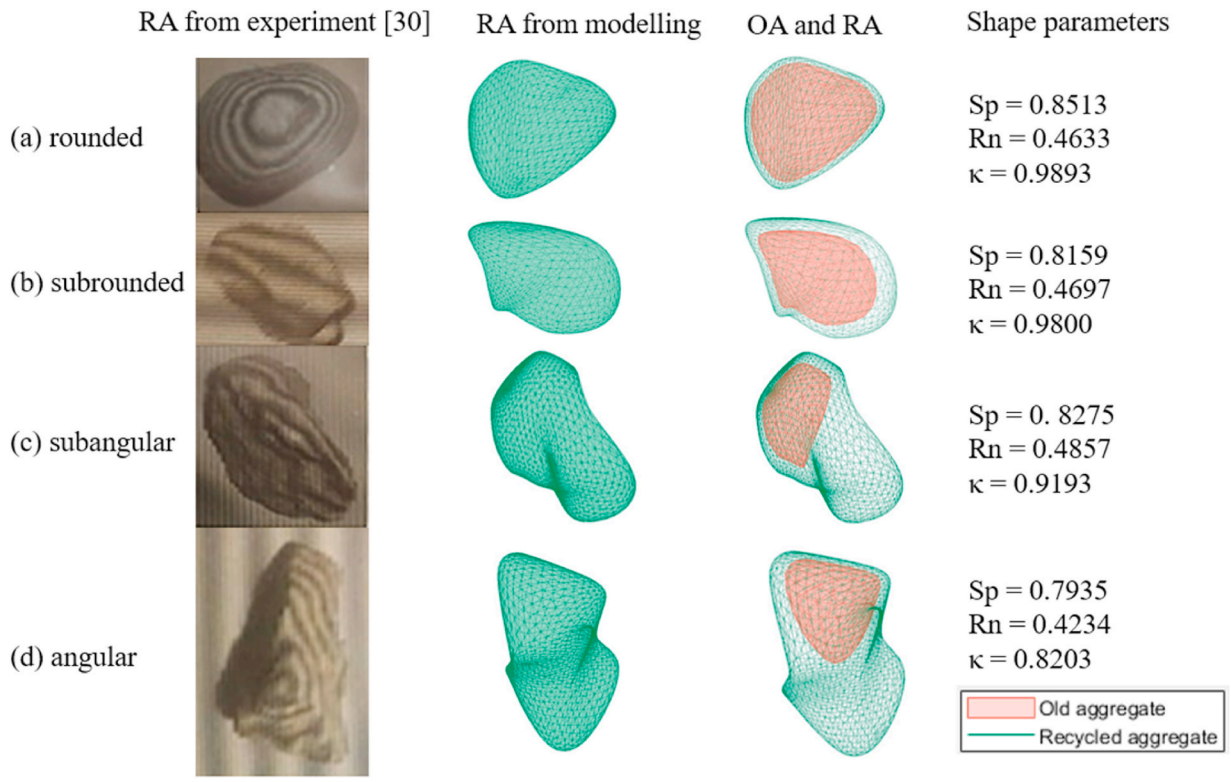

Fig. 18. A comparison of the simulated and characterised individual particles in terms of shape.

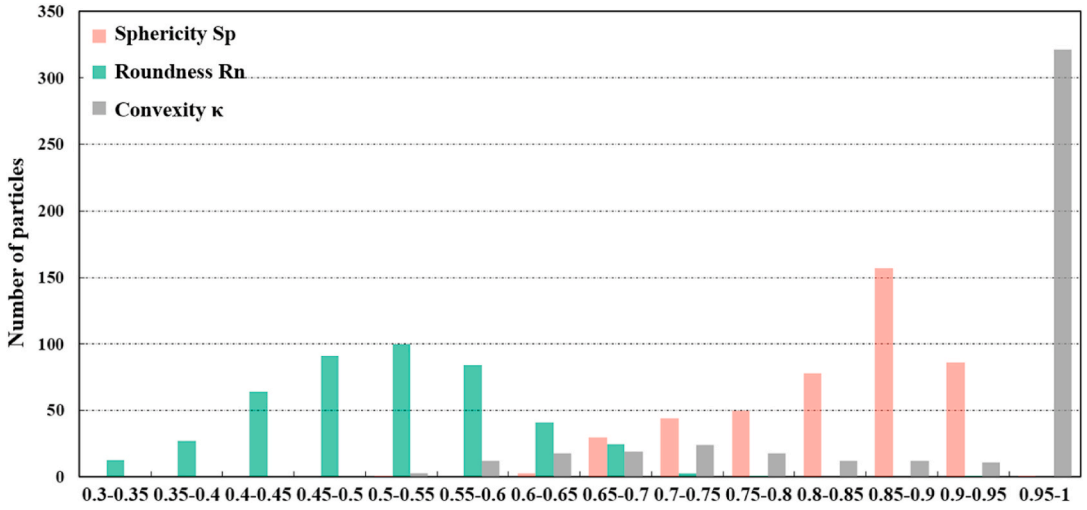

Fig. 19. Parametric analysis of shape of RA particles.

refinement of the old mortar distribution, although its influence on the total volume fraction was comparatively limited. (3) By adjusting the shrinkage ratios of the old aggregate and recycled aggregate cells (Fig. 23), the minimum achievable old mortar content could be reduced, enabling finer control of the lower bounds. A combination of these strategies enabled the model to generate 3D mesostructure with old mortar content closely aligned with the experimental data. This ensures that the simulated 3D mesostructure of RAC can well reflect the inherent variability and provide a reliable foundation for further analysis of mechanical behaviour and damage mechanisms of RAC.

As shown in Tables 3–5, the old mortar content in the generated RAC mesostructure can be effectively controlled through a combination of different parameters, including the volume ratios of the three phases in the first clustering stage, the selection of the second clustering scheme, and the shrinkage ratios applied to the old aggregate and recycled aggregate cells. By systematically adjusting these parameters, the old mortar content in the produced RAC ranges from 18.11 % to 48.86 %, which falls well within the range reported in experimental studies, i.e., 14.3–63.8 %. This demonstrates the flexibility of the proposed modelling framework in capturing the realistic microstructural variability and highlights its applicability for generating representative RAC geometries for further mechanical and fracture simulations.

4. 3D meso-scale modelling of fracture behaviour of RAC

To simulate the fracture behaviour of RAC, a representative volume

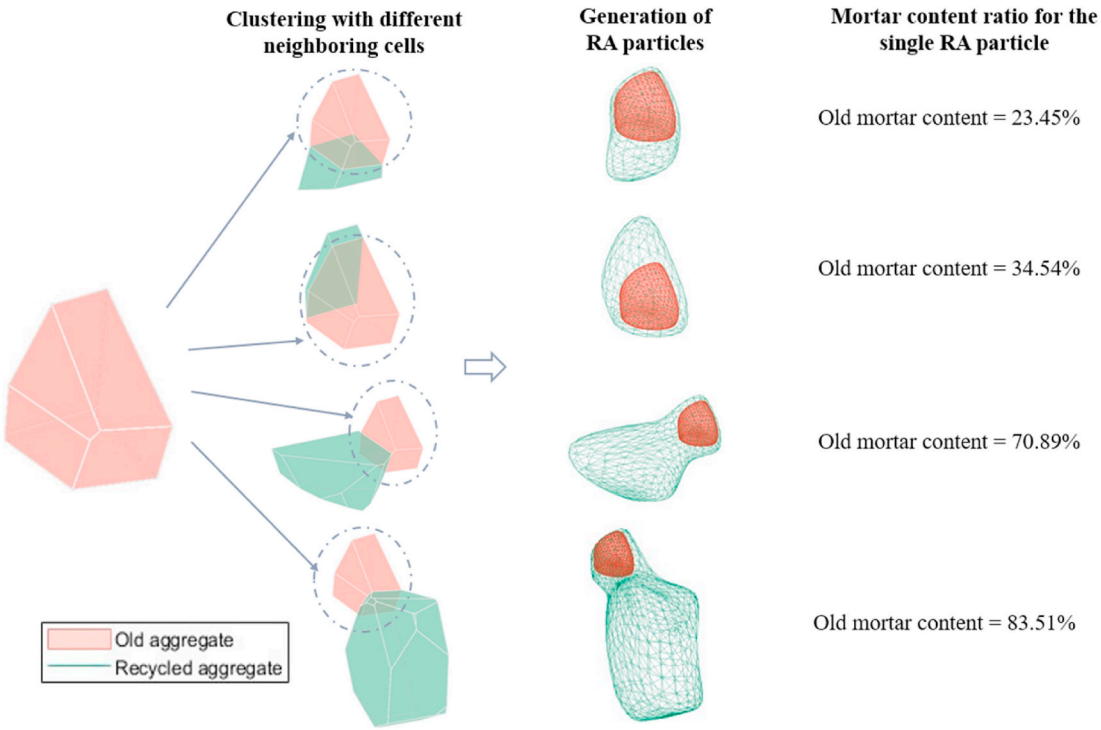

Fig. 20. RAs generated from a single old aggregate cell with various mortar content.

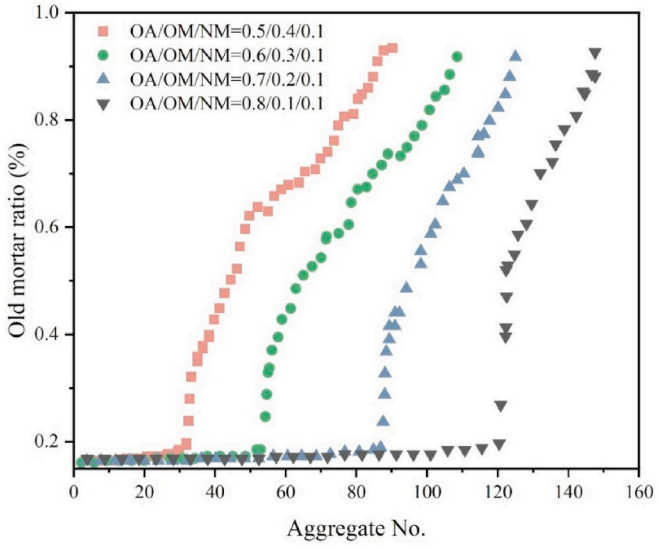

Fig. 21. Effect of the first clustering volume ratios on mortar content in RAC: OA/OM/NM ratio (a) 0.5/0.4/0.1; (b) 0.6/0.3/0.1 (c) 0.7/0.2/0.1; (d) 0.8/0.1/0.1.

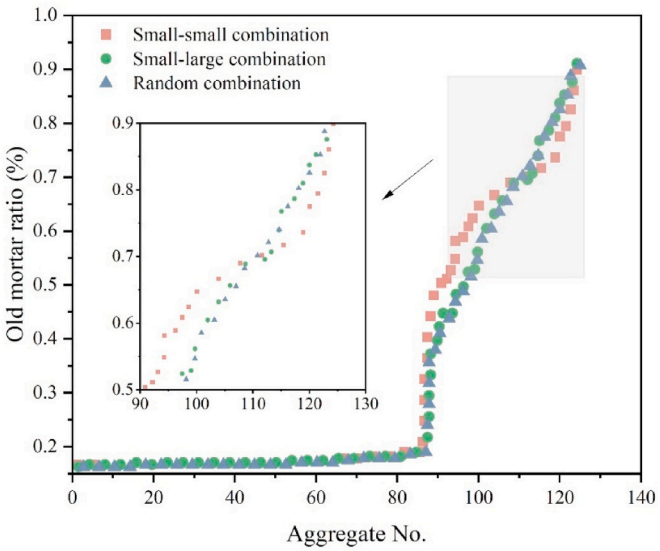

Fig. 22. Effect of the second clustering schemes on mortar content in RAC: (a) Small cells combination with small cells; (b) Small cells combination with large cells; (c) random combination with cells.

element (RVE) with a cubic geometry and side length of 100 mm was constructed to serve as the 3D mesostructure of RAC, consistent with the dimensions commonly adopted for meso-scale modelling of concrete and RAC [25,55]. Corresponding to this size, 128 Voronoi cells were generated to represent individual RA. Recycled coarse aggregates were taken as the modelling object. The PSD of RA for modelling followed the experimental sieve analysis data, where less than 5 % of particles were smaller than 5 mm and over 95 % were within the coarse aggregate range of 5–25 mm (Table 2). As seen in Fig. 16, the target PSD was fitted to achieve a good agreement with the experimental data [49]. The volume fractions of RA and old mortar were set as 37.8 % and 31.5 %, respectively, falling within the ranges reported in literature, i.e., 30–40 % for RA [26,31] and 14.3–63.8 % for old mortar [6,53,54].

It should be noted that cylindrical or prismatic specimens are usually employed to minimise the frictional force between the loading platens and the specimens and experimentally characterise the compressive behaviour of RAC. In this study, cubic RVE of RAC was adopted for meso-scale modelling to facilitate mesh generation, phase distribution, and computational efficiency, following the common practice in meso-scale modelling of concrete [21,26,56–58], in which the friction between the loading platens and the specimens was neglected and thus the specimen geometry has no influence on simulation results and the

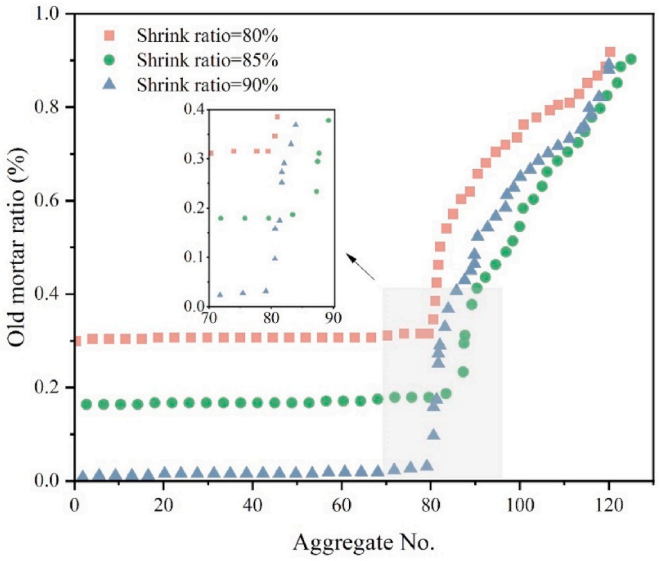

Fig. 23. Effect of shrinkage ratios on mortar content in RAC: shrink ratio (a) 80 %; (b) 85 %; (c) 90 %.

Table 3
Variations in old mortar ratio under different first clustering ratios.

OA/OM/NM ratio in 1st clustering	0.5/0.4/0.1	0.6/0.3/0.1	0.7/0.2/0.1	0.8/0.1/0.1
Clustering scheme	small cells combination with large cells			
Shrinkage ratio of old aggregate cells	85 %			
Shrinkage ratio of recycled aggregate cells	90 %			
Old mortar ratio	**48.86 %**	**41.07 %**	**31.32 %**	**18.11 %**

Table 4
Variation in old mortar ratio under different second clustering schemes.

2nd Clustering scheme	Small cells combination with small cells	Small cells combination with large cells	Random combination with cells
OA/OM/NM ratio in 1st clustering	0.7/0.2/0.1		
Shrinkage ratio of old aggregate cells	85 %		
Shrinkage ratio of recycled aggregate cells	90 %		
Old mortar ratio	**31.98 %**	**31.32 %**	**31.23 %**

simulated compressive behaviour would be comparable to the experimental results. The focus of this study is placed on the compressive behaviour and fracture mechanism accounting for irregular RAC particles, rather than the specimen shape and size effects, which will be considered for future research to further align with experimental practice.

The seeding process followed the workflow described in a previous study [43], beginning with the uniform placement of 3D seed points within the domain. To introduce geometric irregularity, each coordinate was randomly perturbed using a factor of 0.1 and then clamped to remain within the RVE bounds. A shrinking factor of 0.8 was applied to the resulting Voronoi cells to promote inter-particle separation and prevent overlap. Two surface-smoothing (splining) steps were then

Table 5
Variation in old mortar ratio under different shrinkage ratio.

Shrinkage ratio of old aggregate cells	80 %	85 %	90 %
OA/OM/NM ratio in 1st clustering	0.7/0.2/0.1		
2nd Clustering scheme	Random combination with cells		
Shrinkage ratio of recycled aggregate cells	90 %		
Old mortar ratio	**44.76 %**	**31.23 %**	**21.35 %**

performed to refine particle morphology and better replicate the natural irregularity of RA. This procedure introduces controlled geometric variability while preserving target volume fractions, ensuring that the mesostructure is suitable for mechanical and fracture simulations.

4.1. Mesh generation

For OA, OM, and NM, the triangulated mesh surfaces in STL format were imported into ABAQUS, where tetrahedral meshes were generated using the "Convert Tri to Tet" module. The meshing was carried out with C3D4 elements that are 4-node linear tetrahedral elements well-suited for modelling complex and irregular geometries. Zero-thickness cohesive elements were embedded within the tetrahedral mesh formed between phases to represent the ITZs that have a thickness of 10–50 μm, significantly smaller than the characteristic lengths of the aggregates [22]. Especially for RAC, two ITZs would dramatically increase the computational requirements. Cohesive interface elements (CIEs) have been widely utilised and are recognised as an effective method for simulating ITZ in concrete [28,43,48,55,59].

To insert cohesive elements, the interface triangular faces between adjacent phases (i.e., neighbouring faces of OA-OM, and OM-NM) were first identified. The OA-OM neighbouring faces were processed as old ITZ, and the OM-NM neighbouring faces were subsequently assigned as new ITZ. The raw mesh data for the two layers were exported, including node coordinates and element connectivity. Then, for each triangular interface, three node coordinates were copied and assigned with new node numbers to generate the opposing faces of the cohesive layer, taking care to maintain element orientation and continuity (Fig. 24). The original three nodes and the copied nodes were linked to become COH3D6 cohesive elements, with the node ordering reflecting the original and copied surfaces. The cohesive elements were classified as CIE-OLD_ITZ or CIE-NEW_ITZ, depending on whether they are located between OA-OM or OM-NM regions. The new CIE-OLD_ITZ and CIE-NEW_ITZ were saved with the node numbers and connectivity written in the INP file. New nodes were inserted on top of the original nodes, along with the update on the numbering for all nodes, including the C3D4 element mesh as shown in Fig. 24. More details about the creation and insertion of zero-thickness cohesive elements can be found in literature [43,48]. Fig. 25 shows the finite element model of RAC with different phases after meshing.

The bond strength of ITZ was found to be closely associated with the type, shape and surface texture of the aggregate used [58–62]. Variations in the surface texture of coarse aggregates of approximately 4–5 μm (centre line average) result in reduced stress-strain behaviour [63]. Micro-scale geometric features fall outside the scope of this study that only focuses on the meso-scale geometric characteristics. The effects of aggregate surface roughness and micro-texture were not explicitly modelled but were implicitly reflected through the cohesive parameters assigned to the old and new ITZs, which represent the averaged mechanical properties obtained from experiments. This simplification is considered reasonable for capturing the overall mechanical behaviour.

4.2. Material properties

In concrete, aggregates have substantially higher tensile strength compared to mortar and ITZ and thus it is a common simplification to treat aggregates as purely elastic and free from damage, while

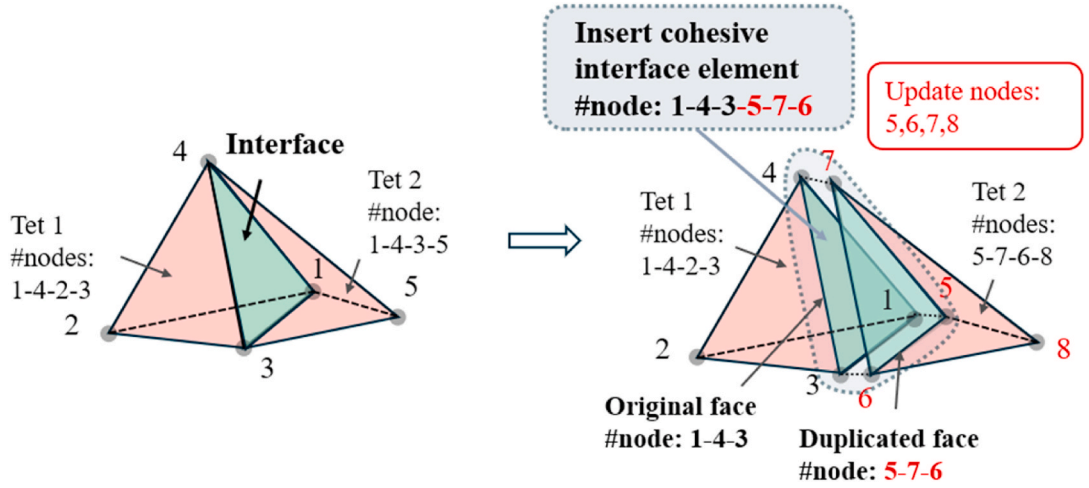

Fig. 24. Insertion of cohesive element at the interface of two tetrahedral elements.

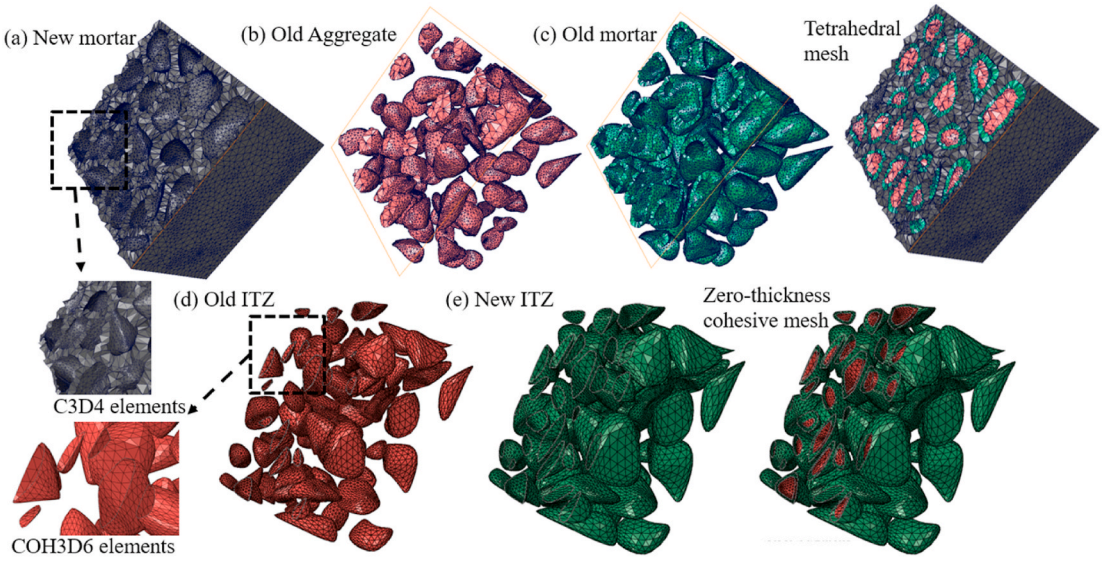

Fig. 25. Finite element model of RAC with different phases after meshing.

microcracks are expected to originate and propagate within mortar and ITZ [25,26,30]. Accordingly, only elastic properties are assigned to all tetrahedral solid elements for aggregates, while concrete damage plasticity (CDP) model [64] was applied to old mortar and new mortar in RAC. Meanwhile, ITZs were modelled using zero-thickness cohesive elements to explicitly simulate the interfacial damage and crack

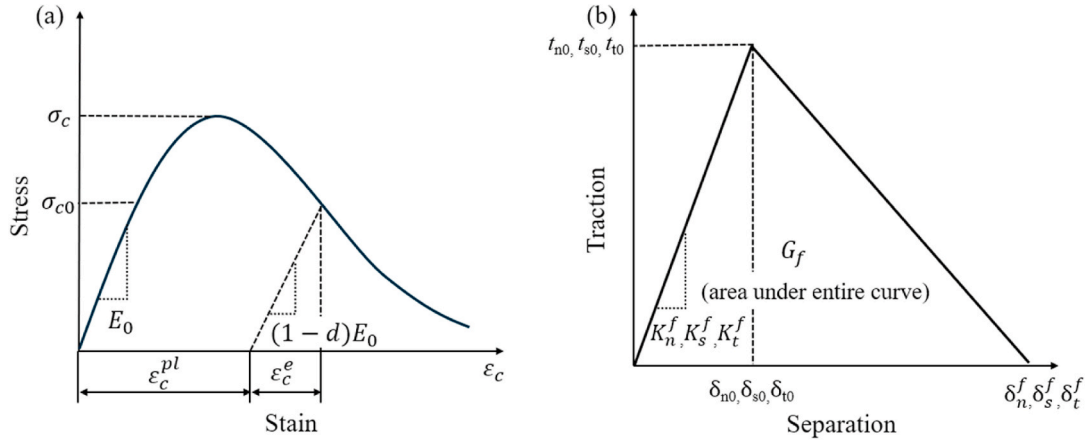

Fig. 26. Constitutive models used in finite element simulations [64]: (a) concrete damage plasticity (CDP) model; (b) cohesive element model.

propagation. As illustrated in Fig. 26, a traction-separation law was employed to characterise the mechanical response of ITZs, where crack initiation was defined using a quadratic nominal stress criterion, accounting for mixed-mode loading conditions [43]. Afterwards, damage evolution was governed by a linear softening law based on fracture energy, enabling progressive stiffness degradation as the separation increased. The cohesive elements were configured with displacement-based damage evolution to accurately capture the localised fracture process of typical concrete, particularly along the mechanically weaker ITZs. Given that the constitutive behaviour of cohesive elements is documented in the ABAQUS User Manual [64] and supporting literature [28,43,48,55,59], only the principal modelling parameters are outlined here.

In this study, the material properties of different phases in RAC including aggregate, old mortar, new mortar, and ITZs obtained from the literature [28,46,48] were adopted for finite element simulations (see Table 6). The old aggregate was modelled with high stiffness and density, consistent with natural coarse aggregates in NAC, while the old and new mortar phases were assigned to lower stiffness and density, given the micro-crack and degradation of old cement paste and the improved integrity of new mortar, respectively. Poisson's ratios for all phases in RAC fall within the typical ranges for cementitious materials. The cohesive interactions were modelled using a linear traction-separation law via the ABAQUS keyword *ELASTIC, TYPE = TRACTION. For both CIE-OLD_ITZ and CIE-NEW_ITZ, the crack initiation follows a quadratic nominal stress criterion, with subsequent linear softening governed by the associated fracture energy. The scalar damage variable (SDEG) was used as the output to quantify the extent of degradation. For the tetrahedral solid elements, elastic modulus and Poisson's ratios were specified for mortar and aggregates. For both types, the same traction-separation formulation was adopted, while different fracture energies were assumed.

The material parameters of RAC were obtained from the experimental studies [8,31,65], while the ITZ parameters were derived from nanoindentation test [8]. The parameters for cohesive elements were adopted from previous interface element-based RAC models [28], confirming their applicability. Minor parameter adjustments were made during preliminary simulations to align the simulated overall stress–strain response of RAC under compression with the experimental data for compressive strength ranges of 25–45 MPa. The calibration with nanoindentation test results indicated that the elastic modulus of ITZs was approximately 70–80 % of that of OM and 80–90 % of that of NM [8]. It was reported that OLD-ITZ had slightly higher strength than NEW-ITZ [31], and thus the corresponding fracture energy and cohesive strength of OLD-ITZ were proportionally increased following the same ratios to maintain consistency with the strength contrast between the two interfaces [28].

Table 6
Material properties of different phases in RAC adopted for numerical simulations.

Material properties	Aggregate	Old mortar	New mortar	OLD_ITZ	NEW_ITZ
Density, ρ (kg/m^3)	2800 [48]	1800 [48],[a]	2200 [48]	2000 [48],[a]	1800 [48],[a]
Young's modulus, E (GPa)	80 [31]	23 [31]	25 [31]	17.5 [25]	16.1 [25]
Compressive strength, f_c (MPa)	–	41.4 [31]	45 [31]	36 [25]	33.1 [25]
Poisson's ratio, ν	0.16 [31]	0.22 [31]	0.22 [31]	0.2 [31]	0.2 [31]
Elastic stiffness K_{n0}, K_{s0}, K_{t0} (MPa/mm)	–	–	–	10^6 [48]	10^6 [48]
Cohesive strength t_{n0}, t_{s0}, t_{t0} (MPa)	–	–	–	2.4 [28,48],[a]	2 [28,48],[a]
Fracture energy, G_f (N/mm)	–	0.14 [28]	0.2 [28]	0.041 [28,48],[a]	0.037 [28,48],[a]

[a] The calibration was conducted based on the ranges reported in the literature and considering the compressive strengths of old ITZ (OLD_ITZ) and new ITZ (NEW_ITZ) as approximately 70–80 % that of old mortar and 80–90 % that of new mortar, respectively [8].

4.3. Loading and boundary conditions

Herein, the mechanical behaviour of RAC under uniaxial compression was modelled using ABAQUS/Explicit, which can effectively simulate the quasi-static behaviour when the loading rate is sufficiently low. A displacement-controlled approach was adopted, where one surface of the RVE was incrementally displaced in the vertical direction while the opposite surface was fully constrained. The simulations proceeded until a maximum displacement of 0.5 mm from top to bottom was reached, as per the literature [29,31,48]. To approximate quasi-static conditions, the displacement was applied using a smooth step amplitude function over a total duration of 0.05 s. This approach can effectively minimise inertial effects and improved numerical stability. The kinetic-to-internal energy ratio was monitored and remained below 5 %, confirming the quasi-static nature of the simulations. Mass scaling with a factor of 5×10^{-6} was applied to increase system mass, allowing larger time increments and reducing computational cost. Sensitivity analyses on mesh element size and loading duration were conducted to balance accuracy and efficiency. These calibrated inputs ensured stable convergence and reliable numerical performance within a practical computational timeframe. The finite element model consisted of around 1,645,343 mesh elements. The simulations were conducted using parallel computing on 16 CPUs, and the loading analysis required about 6 h of runtime. This indicates that, despite the geometric complexity, the proposed modelling framework achieves a balance between realism and computational efficiency, making it suitable for ordinary high-performance desktop or workstation setups.

4.4. Validation

4.4.1. Mesh size

The mesh density analysis was performed to evaluate the influence of element size on the simulation accuracy and convergence of the CDP model. Five finite element configurations with average element sizes from 0.8 mm to 1.6 mm, with 0.2 mm incremental were adopted (Fig. 27). The same geometry model for the specimens with identical

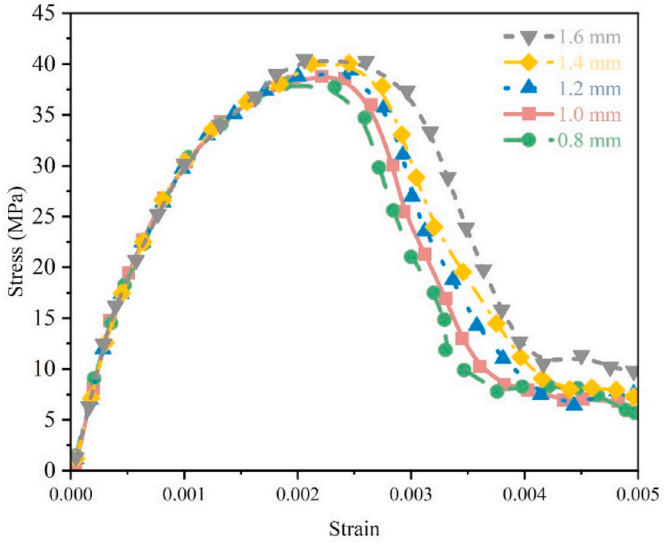

Fig. 27. Compressive stress-strain curves of RAC with various mesh element sizes.

boundary conditions, material parameters, and loading protocols was employed to isolate the effect of mesh density. As the mesh element size increases from 0.8 mm to 1.6 mm, the corresponding peak stress rises from approximately 36.7 MPa–39.8 MPa, and the post-peak softening portion of the stress–strain curve also becomes more pronounced with larger elements. The stress–strain response becomes less sensitive when the element size decreases from 1.2 mm to 0.8 mm compared to that observed from 1.2 mm to 1.6 mm. This suggests that the models with element sizes greater than 1 mm exhibit noticeable discrepancies in accuracy, whereas further refinement below 1 mm yields minimal improvement. Moreover, the number of elements for a 0.8 mm mesh rises by about 80 % compared to that for a 1 mm mesh, leading to a substantially higher computational cost. Therefore, the element size of 1 mm was regarded as the optimal choice for subsequent simulations, offering an appropriate balance between model accuracy and computational efficiency.

4.4.2. Loading rate

The sensitivity analysis of loading time was conducted to find the appropriate loading rate on the quasi-static response and simulation stability for the model. The analysis aimed to ensure that the selected loading rate was sufficiently low to minimise inertial effects while maintaining reasonable computational efficiency. Four loading durations including 0.0125 s (loading rate = 40 mm/s), 0.025 s (loading rate = 20 mm/s), 0.05 s (loading rate = 10 mm/s), and 0.1 s (loading rate = 5 mm/s) were applied under identical boundary and material conditions. The simulation results are presented in Fig. 28, indicating that the influence of loading time becomes more noticeable with the increasing loading rate. As the loading time rises from 0.0125 s to 0. 1 s, the peak stress drops from about 43.2 MPa to 36.8 MPa, suggesting a clear rate-dependent effect. The stress–strain response exhibits pronounced sensitivity when the loading duration is shorter than 0.05 s. Thus, a loading time of 0.05 s was selected as the optimal value for subsequent simulations, considering the balance between computational efficiency and simulation accuracy.

4.4.3. Stress-strain curve

Fig. 29 shows the simulated stress–strain curve of RAC under uniaxial compression in comparison with experimental results collected from literature, in which the RAC specimens with different particle size distribution of aggregates, water-to-cement ratios, compressive strengths, RA treatments, and specimen shapes and dimensions were adopted for measurement, as summarised in Table 7. The simulated stress–strain response consists of the initial elastic stage, peak stress, and post-peak softening behaviour, which falls within the range of experimental results, confirming the simulation reliability. The present model can accurately capture the macroscopic mechanical response of RAC under uniaxial compression within the experimentally observed ranges.

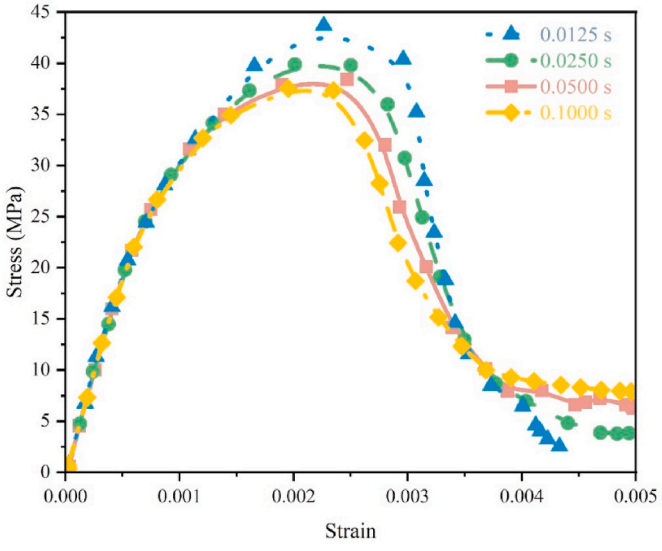

Fig. 28. Stress-strain curves of RAC under uniaxial compression with various loading time.

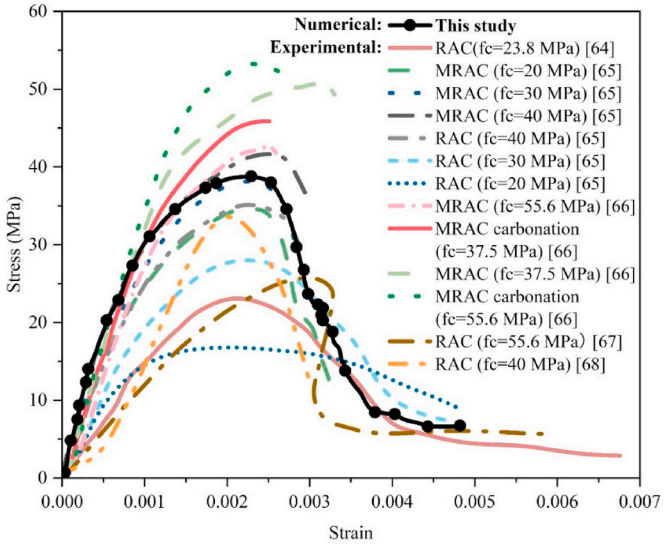

Fig. 29. Comparison of simulation and experimental results of compressive strain-stress curves of RAC.

4.5. Simulation results

Figs. 30–32 present the simulation results of fracture behaviour of RAC under uniaxial compression, capturing the full progression from elastic response to ultimate failure. To explore the crack development patterns, the solid and cohesive elements with a SDEG of 0.9 were assumed to be the failure elements and cracks.

The initial phase of loading (strain $\varepsilon = 0.001$ and $\varepsilon = 0.002$) follows a linear stress–strain relationship with no cracking at the new and old mortar, while the new ITZ has less signs of micro-cracking due to the lower elastic modulus in the old ITZs compared to the adjacent mortar and the new ITZ [8,31]. As the increase of stress beyond the elastic limit ($\varepsilon = 0.003$), the stress–strain curve enters a nonlinear hardening regime (Fig. 29), along with the rise in the damage variable (SDEG) of cohesive elements that represent the old ITZs, indicating the crack initiation. These cracks propagate from the interfaces between recycled aggregates and the old mortar matrix and then extend into old mortar, consistent with the experimental findings [31,55,70]. Crack paths form tortuous networks primarily along the old ITZs and then extend into the old mortar that has lower strength and stiffness than the new mortar. This sequential failure starting from the old ITZ, progressing through old mortar, and eventually reaching new mortar is a typical fracture feature of RAC. After the peak load, the stress drops sharply with further deformation, indicating a brittle failure mode. At this stage, cohesive elements in the most damaged regions reach full degradation, leading to rapid crack coalescence and the formation of a dominant failure surface. The cracks propagate from the ITZs to the old mortar and eventually grow through the new mortar matrix. Fig. 31 shows the local cracks at this loading step, indicating the heterogeneous feature of 3D meso-structure of RAC. There are obviously more failure areas in the old ITZ and new ITZ than mortar phases, along with more damage in the old mortar than new mortar. At the final stage ($\varepsilon = 0.005$), the new and old ITZs have no obvious change till failure as the saturated damage on ITZs had been reached (Fig. 31), while the further crack propagation takes place on old mortar and new mortar until they reach the final failure.

Table 7
A summary of details about RAC specimens adopted for experimental studies in literature.

Ref.	Particle size (mm)	Density (kg/m^3)	w/c ratio	Compressive strength (MPa)	Treatment	Specimen (mm)
[66]	5–31.5	2520	0.43	23.8	Pre-soaked RCA	Prism 100 × 100 × 300 Cube 100 × 100 × 100
[65]	MRAC: OA:28/OM:5 RAC:5-30	2500	0.36/0.45/0.55	20/30/40	Pre-soaked RCA	Cube 150 × 150 × 150
[67]	MRAC: OA:28/OM:5	3150	0.5 (M1) 0.6 (M2)	37.5 (M1) 55.6 (M2)	Carbonated RCA	Cylinders 40 × 40 × 30
[68]	4.75–10	2634	0.521	25.56	Microbial self-healing	Cube 100 × 100 × 100
[69]	5–25	2512	0.45	C40	Elevated temperatures (25–800 °C)	Cube 100 × 100 × 100 Prism 100 × 100 × 300

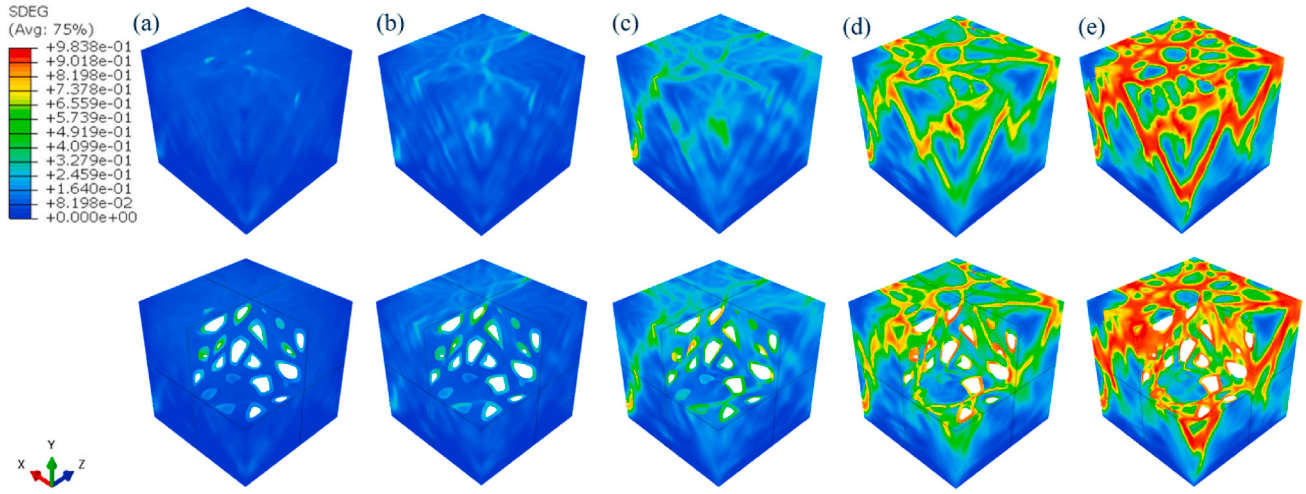

Fig. 30. Fracture processes in RAC under uniaxial compression at: (a) ε = 0.001; (b) ε = 0.002; (c) ε = 0.003; (d) ε = 0.004; and (e) ε = 0.005.

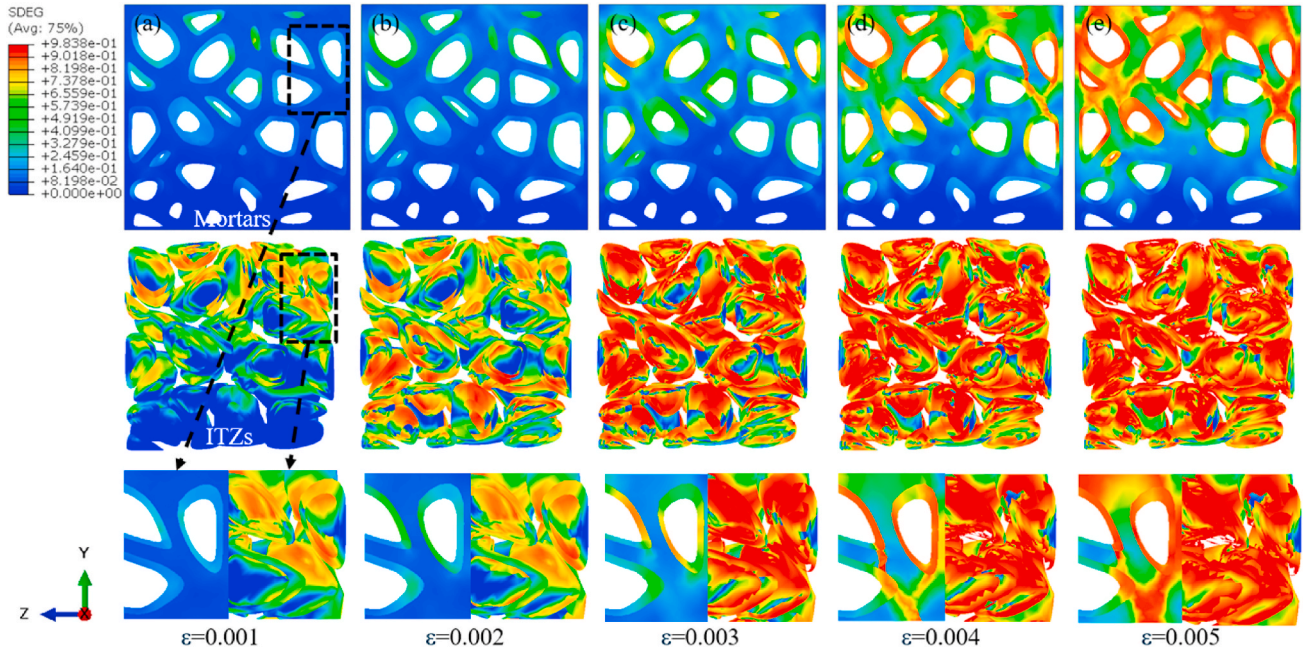

Fig. 31. Cross-section view for fracture processes in RAC under uniaxial compression at: (a) ε = 0.001; (b) ε = 0.002; (c) ε = 0.003; (d) ε = 0.004; (e) ε = 0.005.

Aggregate morphology is a key factor affecting the fracture process [46]. In the present numerical simulations, RA with random variations in irregularity, width, and aspect ratio were incorporated to adequately capture the meso-scale heterogeneity of RA. Irregular shapes of RA with locally small surface areas or pronounced angularity can significantly intensify the local stress concentration and promote the initiation and propagation of microcracks in RAC, as seen in Fig. 32(e). Regarding the final failure pattern, the inclined shear bands at 30°–45° to the loading

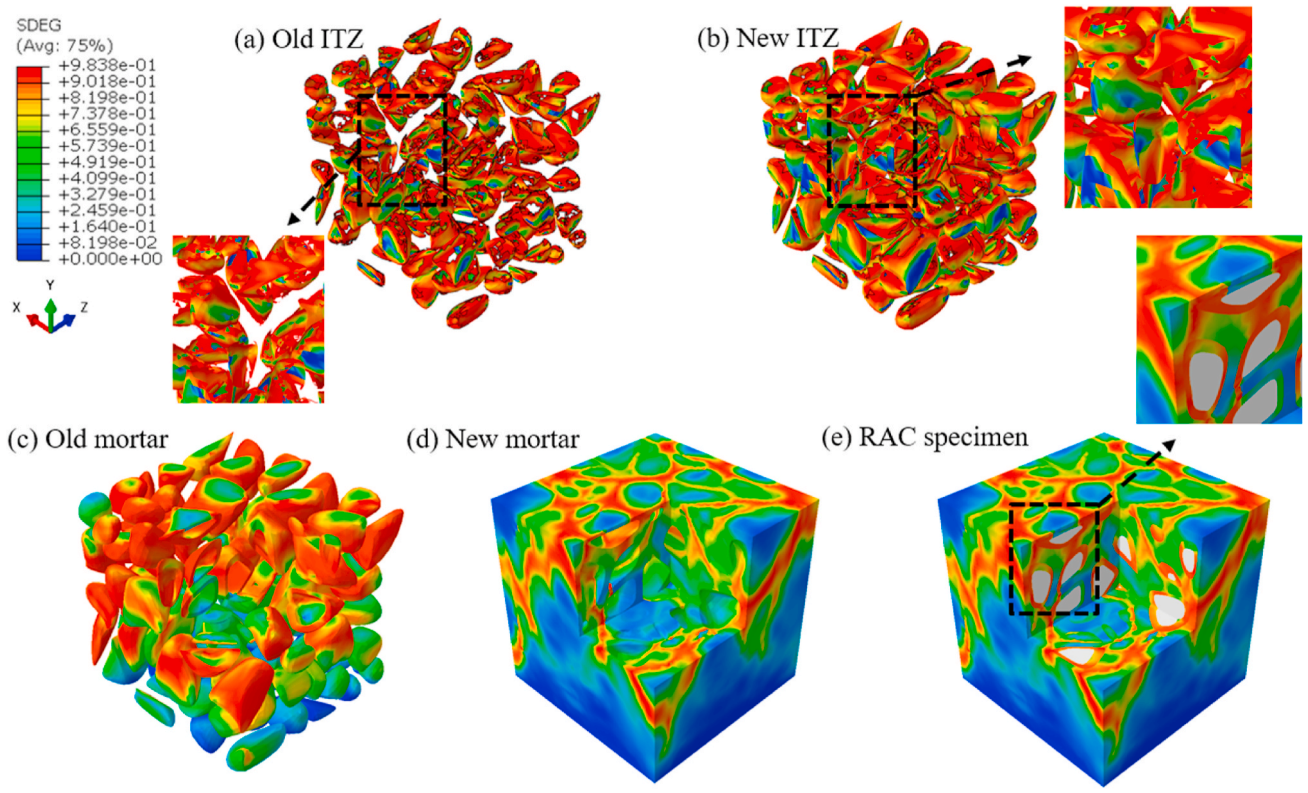

Fig. 32. Cross-section view of fracture in RAC under uniaxial compression at $\varepsilon = 0.004$: (a) Old ITZ; (b) New ITZ; (c) Old mortar; (d) New mortar; (e) RAC.

axis can be found, following the typical patterns of compressive failure of concrete [31,71].

5. Conclusions

In this study, a novel framework for modelling the realistic 3D mesostructure of RAC based on a 3D Voronoi tessellation approach and fracture behaviour of RAC was proposed. It enables efficient generation of irregularly-shaped recycled concrete aggregates, variable old mortar layers, and ITZs in RAC within a fully programmable and flexible modelling platform. By integrating hierarchical clustering, splining, geometric scaling, and zero-thickness cohesive elements, the proposed model can accurately replicate the key features of 3D mesostructure without the need for overlap detection or high computational cost. The simulated mesostructure shows a good agreement with experimental results in terms of shape and size distribution of recycled aggregates as well as old mortar content. Afterwards, the meso-scale modelling of fracture behaviour of RAC can be conducted to gain insights into the damage evolution in RAC under different loading conditions, e.g., uniaxial compression herein, including crack initiation in old ITZs, crack propagation through new ITZs, old mortar and new mortar, and final failure via shear-dominated macro-cracking. The explicit use of cohesive elements enables to capture the interfacial fracture and hierarchical failure mechanisms, indicating the predictive capability and computational efficiency of the proposed model.

Several limitations should be mentioned. First, in the current model, each RA is composed of an OA fully encapsulated by OM. The simplified assumption that OM encloses OA was adopted, consistent with the common practice in meso-scale modelling of RAC [17,21,23,26,31,32]. The mechanical strength is different between OM incompletely enclosed OA and fully enclosed OA [29]. Thus, subsequent work will extend the modelling framework to simulate states where OM partially envelops NA, establish a coexistence model for RA and NA, and conduct sensitivity analysis on the replacement ratio of RA. At that stage, an additional ITZ (OA-NM) will be introduced. Furthermore, a parametric sensitivity analysis of the RA geometry will be performed to quantify the effect of aggregate shapes on mechanical and fracture behaviour of RAC. Second, the ITZs were represented by zero-thickness cohesive elements [17,28,72], which provides an appropriate balance between realism and computational efficiency. The cohesive elements can efficiently capture interfacial debonding and crack propagation but cannot describe the gradual internal damage evolution in ITZs. When computing power is sufficient, the outer layer (i.e., ITZ) can be generated based on the centroids of RAs using the scaling process mentioned above (Section 2.5). The realistic thickness and simulated surface roughness of ITZs can deliver more authentic simulations of mechanical behaviour.

For future work, the incorporation of machine learning techniques will be employed as it may enable efficient generative mesostructure model, surrogate mechanical model and data-driven design optimisation. Moreover, a systematic parametric study and stochastic modelling will be carried out to explore the mesostructure-property relationships in RAC as well as fibre reinforced concrete and RAC by embedding discrete fibres and considering the fibre-matrix interaction, under static and dynamic loadings. This is the subject of ongoing research, which will be presented in future publications.

CRediT authorship contribution statement

Yi Ding: Writing – original draft, Visualization, Validation, Methodology, Investigation, Formal analysis, Data curation, Conceptualization. **Sadjad Naderi:** Writing – review & editing, Methodology. **Gert van der Heijden:** Writing – review & editing. **Mingzhong Zhang:** Writing – review & editing, Supervision, Project administration, Conceptualization.

Declaration of competing interest

The authors declare that they have no known competing financial

interests or personal relationships that could have appeared to influence the work reported in this paper.

Acknowledgements

The authors gratefully acknowledge the financial support from the Royal Society (Award No. IEC\NSFC\233679) and University College London through the Global Engagement Funds.

Data availability

Data will be made available on request.

References

[1] M. Sabbrojjaman, Y. Liu, T. Tafsirojjaman, A comparative review on the utilisation of recycled waste glass, ceramic and rubber as fine aggregate on high performance concrete: mechanical and durability properties, Developments in the Built Environment 17 (2024) 100371, https://doi.org/10.1016/j.dibe.2024.100371.
[2] V.W.Y. Tam, M. Soomro, A.C.J. Evangelista, A review of recycled aggregate in concrete applications (2000–2017), Constr. Build. Mater. 172 (2018) 272–292, https://doi.org/10.1016/j.conbuildmat.2018.03.240.
[3] S.A. Zaidi, M.A. Khan, T. Naqvi, A review on the properties of recycled aggregate concrete (RAC) modified with nano-silica, Mater. Today Proc. (2023), https://doi.org/10.1016/j.matpr.2023.03.674.
[4] J. Yang, Q. Du, Y. Bao, Concrete with recycled concrete aggregate and crushed clay bricks, Constr. Build. Mater. 25 (2011) 1935–1945, https://doi.org/10.1016/j.conbuildmat.2010.11.063.
[5] M.S. de Juan, P.A. Gutiérrez, Study on the influence of attached mortar content on the properties of recycled concrete aggregate, Constr. Build. Mater. 23 (2009) 872–877, https://doi.org/10.1016/j.conbuildmat.2008.04.012.
[6] Y. Fan, J. Xiao, V.W.Y. Tam, Effect of old attached mortar on the creep of recycled aggregate concrete, Struct. Concr. 15 (2014) 169–178, https://doi.org/10.1002/suco.201300055.
[7] D.S. Seo, H.B. Choi, Effects of the old cement mortar attached to the recycled aggregate surface on the bond characteristics between aggregate and cement mortar, Constr. Build. Mater. 59 (2014) 72–77, https://doi.org/10.1016/j.conbuildmat.2014.02.047.
[8] J. Xiao, W. Li, Z. Sun, D.A. Lange, S.P. Shah, Properties of interfacial transition zones in recycled aggregate concrete tested by nanoindentation, Cement Concr. Compos. 37 (2013) 276–292, https://doi.org/10.1016/j.cemconcomp.2013.01.006.
[9] A.G. Khoshkenari, P. Shafigh, M. Moghimi, H.B. Mahmud, The role of 0–2mm fine recycled concrete aggregate on the compressive and splitting tensile strengths of recycled concrete aggregate concrete, Mater. Des. 64 (2014) 345–354, https://doi.org/10.1016/j.matdes.2014.07.048.
[10] S. Arora, S.P. Singh, Analysis of flexural fatigue failure of concrete made with 100% coarse recycled concrete aggregates, Constr. Build. Mater. 102 (2016) 782–791, https://doi.org/10.1016/j.conbuildmat.2015.10.098.
[11] W.H. Bai, B.X. Sun, Experimental study on flexural behavior of recycled coarse aggregate concrete beam, Appl. Mech. Mater. 29–32 (2010) 543–548, https://doi.org/10.4028/www.scientific.net/AMM.29-32.543.
[12] D. Tal, J. Fish, Stochastic multiscale modeling and simulation framework for concrete, Cement Concr. Compos. 90 (2018) 61–81, https://doi.org/10.1016/j.cemconcomp.2018.03.016.
[13] Q. Ren, J. Pacheco, J. de Brito, Methods for the modelling of concrete mesostructures: a critical review, Constr. Build. Mater. 408 (2023) 133570, https://doi.org/10.1016/j.conbuildmat.2023.133570.
[14] C. Liu, M. Zhang, Multiscale modelling of ionic diffusivity in unsaturated concrete accounting for its hierarchical microstructure, Cement Concr. Res. 156 (2022) 106766, https://doi.org/10.1016/j.cemconres.2022.106766.
[15] J. Nikolić, N. Tošić, J. Murcia-Delso, S.M. Kostić, Comprehensive review of the structural behaviour and numerical modelling of recycled aggregate concrete-filled steel tubes, Eng. Struct. 303 (2024) 117514, https://doi.org/10.1016/j.engstruct.2024.117514.
[16] W.C. Zhu, C.A. Tang, Numerical simulation on shear fracture process of concrete using mesoscopic mechanical model, Constr. Build. Mater. 16 (2002) 453–463, https://doi.org/10.1016/S0950-0618(02)00096-X.
[17] Y. Yu, Y. Zheng, Y. Guo, S. Hu, K. Hua, Mesoscale finite element modeling of recycled aggregate concrete under axial tension, Constr. Build. Mater. 266 (2021) 121002, https://doi.org/10.1016/j.conbuildmat.2020.121002.
[18] Murshida, P. Jiyad, P. Nagarajan, Development of mesoscopic model for concrete – a critical review, Mater. Today Proc. (2023), https://doi.org/10.1016/j.matpr.2023.03.709. S2214785323017777.
[19] A. Caggiano, H. Xargay, P. Folino, E. Martinelli, Experimental and numerical characterization of the bond behavior of steel fibers recovered from waste tires embedded in cementitious matrices, Cement Concr. Compos. 62 (2015) 146–155, https://doi.org/10.1016/j.cemconcomp.2015.04.015.
[20] F. de Andrade Salgado, F. de Andrade Silva, Recycled aggregates from construction and demolition waste towards an application on structural concrete: a review, J. Build. Eng. 52 (2022) 104452, https://doi.org/10.1016/j.jobe.2022.104452.
[21] Z. Hu, M. Li-Xuan, J. Xia, J. Liu, J. Gao, J. Yang, Q. Liu, Five-phase modelling for effective diffusion coefficient of chlorides in recycled concrete, Mag. Concr. Res. 70 (2018) 583–594, https://doi.org/10.1680/jmacr.17.00194.
[22] P.S.M. Thilakarathna, K.S. Kristombu Baduge, P. Mendis, V. Vimonsatit, H. Lee, Mesoscale modelling of concrete – a review of geometry generation, placing algorithms, constitutive relations and applications, Eng. Fract. Mech. 231 (2020) 106974, https://doi.org/10.1016/j.engfracmech.2020.106974.
[23] Y. Wu, J. Xiao, Multiscale digital-image driven stochastic finite element modeling of chloride diffusion in recycled aggregate concrete, Constr. Build. Mater. 162 (2018) 239–252, https://doi.org/10.1016/j.conbuildmat.2017.12.024.
[24] X.-Q. Zhou, L.-C. Xie, Mesoscale modelling of recycled aggregate concrete under uniaxial compression of different strain rates, Adv. Struct. Eng. 25 (2022) 1178–1193, https://doi.org/10.1177/13694332211066404.
[25] J. Anuruddh, A. Matthew P, J.B. Matthe J, Generation and numerical analysis of random aggregate structures in recycled concrete aggregate systems, J. Mater. Civ. Eng. 32 (2020), https://doi.org/10.1061/(ASCE)MT.1943-5533.0003113.
[26] M. Hosseinzadeh, M. Dehestani, E. Alizadeh, Three-dimensional multiscale simulations of recycled aggregate concrete employing energy homogenization and finite element approaches, Constr. Build. Mater. 328 (2022) 127110, https://doi.org/10.1016/j.conbuildmat.2022.127110.
[27] Q. Ren, J. Pacheco, J. de Brito, 3D mesoscale modelling of recycled aggregate concrete, Constr. Build. Mater. 411 (2024) 134430, https://doi.org/10.1016/j.conbuildmat.2023.134430.
[28] E.A. Rodrigues, M. Gimenes, L.A.G. Bitencourt Jr., O.L. Manzoli, A concurrent multiscale approach for modeling recycled aggregate concrete, Constr. Build. Mater. 267 (2021) 121040, https://doi.org/10.1016/j.conbuildmat.2020.121040.
[29] Q. Ren, J. Pacheco, J. de Brito, J. Hu, Analysis of the influence of the attached mortar's geometry on the mechanical behaviour of recycled aggregate concrete through mesoscale modelling, Eng. Fract. Mech. 297 (2024) 109876, https://doi.org/10.1016/j.engfracmech.2024.109876.
[30] D. Lin, J. Wu, P. Yan, Y. Chen, Effect of residual mortar on compressive properties of modeled recycled coarse aggregate concrete, Constr. Build. Mater. 402 (2023) 132511, https://doi.org/10.1016/j.conbuildmat.2023.132511.
[31] J. Xiao, W. Li, D.J. Corr, S.P. Shah, Effects of interfacial transition zones on the stress–strain behavior of modeled recycled aggregate concrete, Cement Concr. Res. 52 (2013) 82–99, https://doi.org/10.1016/j.cemconres.2013.05.004.
[32] M. Guo, F. Grondin, A. Loukili, Numerical analysis of the failure of recycled aggregate concrete by considering the random composition of old attached mortar, J. Build. Eng. 28 (2020) 101040, https://doi.org/10.1016/j.jobe.2019.101040.
[33] H.G. Gebremariam, S. Taye, A.G. Tarekegn, Parent concrete strength effects on the quality of recycled aggregate concrete: a review, Heliyon 10 (2024) e26212, https://doi.org/10.1016/j.heliyon.2024.e26212.
[34] M. Bravo, J. de Brito, J. Pontes, L. Evangelista, Mechanical performance of concrete made with aggregates from construction and demolition waste recycling plants, J. Clean. Prod. 99 (2015) 59–74, https://doi.org/10.1016/j.jclepro.2015.03.012.
[35] C.S. Poon, Z.H. Shui, L. Lam, H. Fok, S.C. Kou, Influence of moisture states of natural and recycled aggregates on the slump and compressive strength of concrete, Cement Concr. Res. 34 (2004) 31–36, https://doi.org/10.1016/S0008-8846(03)00186-8.
[36] K.K. Sagoe-Crentsil, T. Brown, A.H. Taylor, Performance of concrete made with commercially produced coarse recycled concrete aggregate, Cement Concr. Res. 31 (2001) 707–712, https://doi.org/10.1016/S0008-8846(00)00476-2.
[37] S. Barbhuiya, A. Jivkov, B.B. Das, A review of multi-scale modelling of concrete deterioration: fundamentals, techniques and perspectives, Constr. Build. Mater. 406 (2023) 133472, https://doi.org/10.1016/j.conbuildmat.2023.133472.
[38] S. Hentz, F.V. Donzé, L. Daudeville, Discrete element modelling of concrete submitted to dynamic loading at high strain rates, Comput. Struct. 82 (2004) 2509–2524, https://doi.org/10.1016/j.compstruc.2004.05.016.
[39] Z.M. Wang, A.K.H. Kwan, H.C. Chan, Mesoscopic study of concrete I: generation of random aggregate structure and finite element mesh, Comput. Struct. 70 (1999) 533–544, https://doi.org/10.1016/S0045-7949(98)00177-1.
[40] Q. Ren, J. Pacheco, J. de Brito, New generation and separation method for the computational modelling of the mesostructure of concrete, Eng. Fract. Mech. 284 (2023) 109212, https://doi.org/10.1016/j.engfracmech.2023.109212.
[41] P. Wriggers, S.O. Moftah, Mesoscale models for concrete: homogenisation and damage behaviour, Finite Elem. Anal. Des. 42 (2006) 623–636, https://doi.org/10.1016/j.finel.2005.11.008.
[42] Y. Lin, X. Feng, Z. Zhang, Microscopic simulation of thermo-mechanical behaviors in recycled concrete under freeze–thaw action, Constr. Build. Mater. 409 (2023) 133892, https://doi.org/10.1016/j.conbuildmat.2023.133892.
[43] S. Naderi, M. Zhang, An integrated framework for modelling virtual 3D irregulate particulate mesostructure, Powder Technol. 355 (2019) 808–819, https://doi.org/10.1016/j.powtec.2019.07.089.
[44] S. Naderi, M. Zhang, 3D meso-scale modelling of tensile and compressive fracture behaviour of steel fibre reinforced concrete, Compos. Struct. 291 (2022) 115690, https://doi.org/10.1016/j.compstruct.2022.115690.
[45] H. Wang, S. Owyong, A. Shi, S. Shin, T.H. Nguyen, A. Lin, Investigating on thermal insulation in concrete partition wall with insulation-material-infilled voronoi sections: feature impact analysis and efficient assessment approach, J. Build. Eng. 96 (2024) 110437, https://doi.org/10.1016/j.jobe.2024.110437.
[46] S. Naderi, M. Zhang, Meso-scale modelling of static and dynamic tensile fracture of concrete accounting for real-shape aggregates, Cement Concr. Compos. 116 (2021) 103889, https://doi.org/10.1016/j.cemconcomp.2020.103889.
[47] O.K. Hunter, Characterization of Pore Structure and Crack Propagation in Concrete Using x-ray Computed Tomography, M.S., University of Maryland, College Park,

2004. https://www.proquest.com/docview/305174520/abstract/542BFD0434FF4428PQ/1. (Accessed 31 October 2025).
[48] X. Wang, M. Zhang, A.P. Jivkov, Computational technology for analysis of 3D meso-structure effects on damage and failure of concrete, Int. J. Solid Struct. 80 (2016) 310–333, https://doi.org/10.1016/j.ijsolstr.2015.11.018.
[49] L. Butler, J.S. West, S.L. Tighe, Effect of recycled concrete aggregate properties on mixture proportions of structural concrete, Transp. Res. Rec. 2290 (2012) 105–114, https://doi.org/10.3141/2290-14.
[50] B.S. Institution, BS EN 933-1. Tests for Geometrical Properties of Aggregates: Part 1. Determination of Particle Size Distribution. Sieving Method, British Standards Institution, 2021.
[51] J.W. Bullard, E.J. Garboczi, Defining shape measures for 3D star-shaped particles: sphericity, roundness, and dimensions, Powder Technol. 249 (2013) 241–252, https://doi.org/10.1016/j.powtec.2013.08.015.
[52] H. He, L. Courard, E. Pirard, F. Michel, Shape analysis of fine aggregates used for concrete, Image Anal. Stereol. 35 (2016) 159–166, https://doi.org/10.5566/ias.1400.
[53] Z.H. Duan, C.S. Poon, Properties of recycled aggregate concrete made with recycled aggregates with different amounts of old adhered mortars, Mater. Des. 58 (2014) 19–29, https://doi.org/10.1016/j.matdes.2014.01.044.
[54] A. Domingo-Cabo, C. Lázaro, F. López-Gayarre, M.A. Serrano-López, P. Serna, J. O. Castaño-Tabares, Creep and shrinkage of recycled aggregate concrete, Constr. Build. Mater. 23 (2009) 2545–2553, https://doi.org/10.1016/j.conbuildmat.2009.02.018.
[55] J. Wang, A.P. Jivkov, Q.M. Li, D.L. Engelberg, Experimental and numerical investigation of mortar and ITZ parameters in meso-scale models of concrete, Theor. Appl. Fract. Mech. 109 (2020) 102722, https://doi.org/10.1016/j.tafmec.2020.102722.
[56] T. Nguyen, A. Ghazlan, A. Kashani, S. Bordas, T. Ngo, 3D meso-scale modelling of foamed concrete based on X-ray computed tomography, Constr. Build. Mater. 188 (2018) 583–598, https://doi.org/10.1016/j.conbuildmat.2018.08.085.
[57] Z. Yang, W. Ren, R. Sharma, S. McDonald, M. Mostafavi, Y. Vertyagina, T. J. Marrow, In-situ X-ray computed tomography characterisation of 3D fracture evolution and image-based numerical homogenisation of concrete, Cement Concr. Compos. 75 (2017) 74–83, https://doi.org/10.1016/j.cemconcomp.2016.10.001.
[58] Y. Zhang, Q. Chen, Z. Wang, J. Zhang, Z. Wang, Z. Li, 3D mesoscale fracture analysis of concrete under complex loading, Eng. Fract. Mech. 220 (2019) 106646, https://doi.org/10.1016/j.engfracmech.2019.106646.
[59] H. Zhang, Y. Huang, Z. Yang, F. Guo, L. Shen, 3D meso-scale investigation of ultra high performance fibre reinforced concrete (UHPFRC) using cohesive crack model and weibull random field, Constr. Build. Mater. 327 (2022) 127013, https://doi.org/10.1016/j.conbuildmat.2022.127013.
[60] B. Chiaia, J.G.M. van Mier, A. Vervuurt, Crack growth mechanisms in four different concretes: microscopic observations and fractal analysis, Cement Concr. Res. 28 (1998) 103–114, https://doi.org/10.1016/S0008-8846(97)00221-4.
[61] G. Prokopski, J. Halbiniak, Interfacial transition zone in cementitious materials, Cement Concr. Res. 30 (2000) 579–583, https://doi.org/10.1016/S0008-8846(00)00210-6.
[62] T. Akçaoğlu, M. Tokyay, T. Çelik, Assessing the ITZ microcracking via scanning electron microscope and its effect on the failure behavior of concrete, Cement Concr. Res. 35 (2005) 358–363, https://doi.org/10.1016/j.cemconres.2004.05.042.
[63] C. Perry, J.E. Gillott, The influence of mortar-aggregate bond strength on the behaviour of concrete in uniaxial compression, Cement Concr. Res. 7 (1977) 553–564, https://doi.org/10.1016/0008-8846(77)90117-X.
[64] Dassault Systèmes, Abaqus Analysis User's Guide, Version 6.16, Dassault Systèmes Simulia Corp, Providence, RI, 2016.
[65] J. Xiao, W. Li, Z. Sun, S.P. Shah, Crack propagation in recycled aggregate concrete under uniaxial compressive loading, ACI Mater. J. 109 (2012) 451–461, https://doi.org/10.14359/51683920.
[66] J. Xiao, J. Li, Ch Zhang, Mechanical properties of recycled aggregate concrete under uniaxial loading, Cement Concr. Res. 35 (2005) 1187–1194, https://doi.org/10.1016/j.cemconres.2004.09.020.
[67] L. Li, J. Xiao, D. Xuan, C.S. Poon, Effect of carbonation of modeled recycled coarse aggregate on the mechanical properties of modeled recycled aggregate concrete, Cement Concr. Compos. 89 (2018) 169–180, https://doi.org/10.1016/j.cemconcomp.2018.02.018.
[68] J. Xiao, Z. Lv, Z. Duan, C. Zhang, Multi-scale characterization of the 3D printed concrete strength considering the full grade pore structure, Cement Concr. Compos. 164 (2025) 106246, https://doi.org/10.1016/j.cemconcomp.2025.106246.
[69] H. Jian, E. Zhu, W. Cai, Z. Bai, T. Yao, J. Li, Experimental investigation on compressive performance of recycled aggregate concrete (RAC) incorporating diatomite as supplementary cementitious material after exposure to elevated temperatures, Constr. Build. Mater. 493 (2025) 143261, https://doi.org/10.1016/j.conbuildmat.2025.143261.
[70] Q. Liu, J. Xiao, Z. Sun, Experimental study on the failure mechanism of recycled concrete, Cement Concr. Res. 41 (2011) 1050–1057, https://doi.org/10.1016/j.cemconres.2011.06.007.
[71] E. Wu, X. Ma, C. Fang, N. Li, L. Jia, P. Jiang, W. Wang, Strength performance and microscopic mechanism of cement mortar incorporating fine recycled concrete aggregate and natural sand, J. Build. Eng. 100 (2025) 111767, https://doi.org/10.1016/j.jobe.2025.111767.
[72] C. Zhu, E. Zhu, B. Wang, Z. Zhang, M. Li, Mesoscale fracture simulation of recycled aggregate concrete under uniaxial compression based on cohesive zone model, Developments in the Built Environment 19 (2024) 100481, https://doi.org/10.1016/j.dibe.2024.100481.